NASA Contractor Report 4318

A Comparison of Single-Cycle Versus Multiple-Cycle Proof Testing Strategies

S. J. Hudak, Jr., R. C. McClung,
M. L. Bartlett, J. H. FitzGerald,
and D. A. Russell

CONTRACT NAS8-37451
AUGUST 1990

NASA Contractor Report 4318

A Comparison of Single-Cycle Versus Multiple-Cycle Proof Testing Strategies

S. J. Hudak, Jr., R. C. McClung,
M. L. Bartlett, and J. H. FitzGerald
Southwest Research Institute
San Antonio, Texas

D. A. Russell
Rocketdyne Division
Rockwell International Corporation
Canoga Park, California

Prepared for
George C. Marshall Space Flight Center
under Contract NAS8-37451

National Aeronautics and
Space Administration
Office of Management
Scientific and Technical
Information Division

1990

TABLE OF CONTENTS

LIST OF ILLUSTRATIONS

LIST OF ILLUSTRATIONS (Continued)

LIST OF ILLUSTRATIONS (Continued)

LIST OF TABLES

DEFINITION OF SYMBOLS

a	crack size (particularly, maximum depth of a surface crack)
a_{cr}	critical crack size
a_i, a_f	initial and final crack sizes
a_{th}	crack length below which initiation of ductile tearing will not occur during a proof test
Δa	change in crack length (crack growth increment)
A_1, A_2	coefficients in (empirical) power-law description of material resistance curve
A_e	elastic area under the load-displacement curve
A_T	total area under the load-displacement curve
B	specimen thickness
c	half-length (on the surface) of a surface crack
C	empirical coefficient in a Paris Law description of fatigue crack growth, or general constant in empirical models for material resistance curve proposed by Orange
C_M	equivalent compliance of a linear spring placed in series with a cracked body to represent the elastic compliance of the total system
da/dN	average crack growth rate per cycle of loading
E	Young's (elastic) modulus
E'	effective elastic modulus, equal to E for plane stress and $E'/(1-\nu^2)$ for plane strain
F_1, F_2, F_3, F_4	general constants in equations relating applied load to J or to load-line displacement, representing various known functions of specimen geometry, crack length, and material properties
h_0	coefficient in the plastic component of J (typically a function of the strain hardening exponent)
J	value of the J-integral
J_{app}	applied value of the J-integral due to external loading
J_e	elastic component of J
J_{Ic}	critical value of the J-integral
J_{max}	maximum value of the J-integral
J_R	material resistance to crack growth expressed in terms of the J-integral
J_z	contribution to J from effective crack length (plastic zone) correction term

DEFINITION OF SYMBOLS (Continued)

ΔJ	range of the J-integral
K	linear elastic stress intensity factor
K_c	apparent fracture toughness, or critical value of K for fracture
K_{Ic}	fracture toughness (rigorously, the plane strain fracture toughness)
K_{Ie}	linear elastic value of the stress intensity factor (special nomenclature for the equivalent energy J estimation procedure)
K_{max}	maximum value of the applied stress intensity factor
K_R	plasticity-modified stress intensity factor in equivalent energy J estimation procedure
ΔK	range of the stress intensity factor
m	empirical exponent in a Paris Law description of fatigue crack growth
n	strain-hardening exponent in a Ramberg-Osgood constitutive relationship
N	number of loading cycles
N_i, N_f	residual fatigue life of a structural component (associated with crack sizes a_i and a_f, respectively)
P	applied load
R	in general, material resistance to stable crack growth; sometimes denoting a constant in an empirical model for the material resistance curve which identifies a particular value of material resistance
R^σ	cyclic stress ratio, K_{min}/K_{max}
R_x^σ	cyclic stress ratio corresponding to a given fatigue range marker band
t	specimen thickness, especially of a surface-cracked plate
T	general constant in empirical models for material resistance curve proposed by Orange, identifying the asymptotic slope of the tearing portion of the curve
w	specimen width, especially of a surface-cracked plate
α	coefficient on stress term in Ramberg-Osgood constitutive equation
Δ	load-line displacement of a cracked body neglecting any system compliance.
Δ_T	total load-line displacement of a cracked body, including contributions from system compliance

DEFINITION OF SYMBOLS (Continued)

ε	strain
ε_0	strain constant in a Ramberg-Osgood constitutive equation
ε_p	plastic strain
ε_{ref}	reference strain in CEGB *J* estimation procedure
μ_x	mean value of a log-normal distribution
ν	Poisson's ratio
σ	stress
σ_0	stress constant in a Ramberg-Osgood constitutive equation, generally set equal to the yield stress or flow stress
σ_∞	remote applied stress
σ_c	critical stress for unstable fracture
σ_p	applied stress in a proof test
σ_r	residual strength of a structural component
σ_{ref}	reference stress in CEGB *J* estimation procedure
σ_{ult}	ultimate strength of a material
σ_x	standard deviation of a log-normal distribution
σ_{ys}	yield strength of a material

NONSTANDARD ABBREVIATIONS

CEGB	Central Electricity Generating Board (United Kingdom)
COD	Crack Opening Displacement
CT	Compact Tension fracture mechanics specimen
EDM	Electro-Discharge Machining
EPRI	Electric Power Research Institute
MCPT	Multiple Cycle Proof Testing
NDE	Nondestructive Evaluation
PDF	Probability Distribution Function
SSME	Space Shuttle Main Engine
SwRI	Southwest Research Institute

1. INTRODUCTION

Although proof testing is generally not the preferred method of crack detection, it has proven useful as a supplement to conventional nondestructive evaluation (NDE) methods, particularly when NDE is compromised by geometric complexities of the component, or structure. The objective of proof testing is to screen out gross manufacturing or material deficiencies and therefore provide additional quality assurance of delivered hardware. It is in this spirit that Rocketdyne has utilized proof testing on components of the Space Shuttle Main Engine (SSME). In this case, Rocketdyne has applied a modified version of conventional single-cycle proof testing which involves multi-cycle proof testing (MCPT). Typically, only pressure loads are applied during the proof test, and thus simulation of actual pressure distributions in components with internal pressure gradients is only approximate. To compensate for the fact that all service conditions are not simulated (for example, thermal or mechanical loading), the operating pressure is generally scaled-up by a proof factor of 1.2. Proof testing typically occurs prior to service, but in special cases it is also utilized as part of an in-service or recycle inspection. Based on demonstrated success on a number of propulsion systems over the years, five-cycle proof testing has been adopted as a standard practice by Rocketdyne.

Potential benefits of proof testing must always be weighed against the possibility of inflicting additional undetected damage on the component through subcritical crack growth or stable tearing upon loading. The decision as to whether or not to use proof testing for the purpose of flaw screening, as well as the development of an optimum strategy for such testing, requires appropriate fracture mechanics analysis. Since the application of proof testing to brittle materials results in little or no stable crack growth on loading, multi-cycle proof testing is unnecessary, and the relevant fracture mechanics analysis is relatively straightforward. On the other hand, multi-cycle proof testing is generally applied to tougher materials which often exhibit significant stable crack growth on loading, and the relevant fracture mechanics analysis can be considerably more complex. Although these techniques have been outlined [1,2,3], certain underlying concepts remain unproven and the appropriate fracture mechanics material properties, needed to characterize the propensity for stable crack growth, are generally not available.

The overall objective of this program is to assess the relative advantages and disadvantages of single-cycle versus multi-cycle proof testing. Initially, consideration was given to approaching this problem empirically. However, it became evident that because of the many complications involved, such an approach would not provide a generally applicable answer to the problem at hand. Thus, efforts were redirected towards the formulation of an analytical model for MCPT which could be used to elucidate the interaction of key variables--specifically, component crack size distribution, the character of the material resistance curve, and elastic-plastic loading conditions. Selected experiments were also conducted to explore the nature of surface crack growth in Inconel 718, as well as to provide the material properties needed to implement the analytical model. For similar reasons, information on the crack size distribution in SSME components, as well as in Inconel 718 castings and weldments was also compiled and statistically analyzed.

2. TECHNICAL BACKGROUND

The intent of this section is to outline relevant background information on MCPT and to briefly describe concepts which are important to developing an understanding of MCPT, as well as to formulating an analytical model for this process.

2.1 Rocketdyne Multi-cycle Proof Testing Experience

Multi-cycle proof testing of pressurized components has been selectively implemented by Rocketdyne since 1952. Prior to that time, the more conventional practice of single-cycle proof testing was employed. Multi-cycle proof testing originated as the result of component failures on the NALAR program at pressures significantly less than the initial hydrostatic proof. Failures were experienced as low as 46% of proof pressure. Although the failure investigation did not explain the cause of the phenomenon, it was recommended that five-cycle proof testing with 10-second hold times be incorporated to eliminate deficient hardware. The current procedure for multi-cycle proof testing on the SSME consists of the application of five proof cycles at a minimum pressure of 1.2 times the maximum operating pressure, each with a minimum hold time of 30 seconds. The proof pressure is selected to keep nominal stresses below 85% of the material's ultimate strength as well as low enough to preclude detrimental yielding, although localized yielding can sometimes occur. Application of five-cycle proof testing at Rocketdyne has expanded to most production programs.

Since the inception of the multi-cycle test, proof pressure testing has supported the fact that component failures can be experienced on the second, third, fourth, or fifth cycles at lower pressures than applied on the first cycle. These failures generally initiated from undetected flaws in the component. This finding illustrates a potential deficiency in the conventional single-cycle test and poses a challenge to determine optimum strategies for proof testing.

The primary justification for five-cycle proof testing, in particular, is the successful record of performance of Rocketdyne engines and the lack of service failures of pressurized components whenever this procedure has been implemented. This experience includes those cases where components have passed the first cycle of pressurization of a five-cycle proof test only to fail on a subsequent proof pressure cycle at or below full pressure. As indicated in Tables 1 and 2 [4], many of these cases, documented prior to 1979, involved components of the SSME. In several cases the hardware deficiencies, revealed after having passed the first proof pressure cycle, were judged to present a significant risk of component failure or malfunction in service. This direct hardware experience is further evidence of the potential benefit arising from the implementation of MCPT. As one might expect, the highest incidence of proof test failures has occurred in components with the lowest design margin.

TABLE 1

SUMMARY OF FIVE-CYCLE PROOF TESTS (Pre-1979) FOR CASES IN WHICH PRE-EXISTING DEFECT WAS IDENTIFIED

(Note: Does not include those instances where failure occurred on the 1st proof cycle)

Program	Component	Material	Failure Cycle	% Proof Pres. at Failure	Component Thickness, in.	Defect Information (dimensions in inches)
SSME	LPOTP Housing	Tens-50	4	80%	---	Casting Defect
SSME	Nozzle Mixer Bowl	Inconel 718	2,3	Leak	---	Casting Porosity
SSME	Turbine Disch. Duct Bellows Assy	Inconel 718	2	56%	~.030	Weld Porosity
SSME	High Press. Fuel Duct	Ti 5-2.5	4 (Cryo)	100% @ 5 Sec	.133	I.D. Axial (HAZ)
SSME	Fuel Turb. Drive Duct	Inconel 718	2	75%	---	Cracks at Lugs
SSME	Powerhead Preburner Fuel Supply Duct	Incoloy 903	5	100%	.145	.08 x 1.1 Non-Metallic Inclusion
SSME	Flight Nozzle Tubes	A-286	2, 3, 4, 5 3 Examples	Various 72% 80% 100% (12 sec hold)	~.010 .010 .0105 .010	.007 x .070 .006 x .180 .007 x .060
F-1 F-1	Thrust Chamber Tubes MK-10 Fuel Volute Casting	Inco X-750 Tens-50	3 5	61% 100% (Depressurization) from	.018 .600	.0057 x Long Lap .09 x .31 Inclusion (1% Permanent Deformation at Splitter Leading Edge)
RS-27	Turbopump Fuel Inlet Elbow	6061 Al	2 (4 Incidents)	100%	---	Vane Fillet Cracks

TABLE 2

SUMMARY OF MULTI-CYCLE PROOF TESTS (Pre-1979) FOR CASES IN WHICH PRE-EXISTING DEFECT COULD NOT BE POSITIVELY IDENTIFIED

(Note: Does not include instances where failure occurred on the 1st proof cycle)

Program	Component	Material	Failure Cycle	% Proof Pres. at Failure	Component Thickness, in.
Nalar	Helium Bottle	4130 Bar	Numerous Post Proof	Down to 46%	.071-.081
Thor	Gas Generator Blade Valve HSG	356-T6Al	5	78%	---
Atlas MA-5	Turbine Inlet Manifold Nut	300 Series Cres	3	100%	---
SSME	Nozzle Tee	Inconel 718	2	---	---
SSME	HPFTP Bellows Assy	---	N/A	100%	---
SSME	HPOTP Bellows	---	N/A	100%	---
SSME	Main Injector	Inconel 718	2	100%	---
SSME	Oxid. Tank Pressurant Short Bellows	Inconel 718	2, 4	100%	---
SSME	HPFTP Inlet	Ti 5-2.5	3	100%	---

Table 1 contains a summary of proof failures after the first cycle where a defect was positively identified as the cause of failure. Where details were found identifying the defect size, it can be seen that the defects were generally large compared to the thickness and many times the thickness in length. This observation, coupled with the MK-10 volute casting defect located in a high strain region, implies that significant local plastic deformation may have occurred prior to failure. Therefore, even though proof limits are selected so that the components remain nominally elastic, plastic deformation in the uncracked ligament may have been a contributing factor to the multi-cycle proof failures. Table 2 lists additional instances where proof failures occurred after the first cycle, but identification of the cause of failure could not be related conclusively to a pre-existing defect.

One immediate observation from Tables 1 and 2 is that multi-cycle proof failures were not isolated to a particular material or material system, but were observed to occur in a broad range of materials. It is also significant to note that many of the components listed contain relatively thin sections. This observation is consistent with a propensity for thin sections to exhibit stable crack growth on loading, as will be discussed later in terms of R-curve behavior. Finally, the fact that the defect depth tended to be large compared to the thickness may contribute to a loss of constraint for the normally highly constrained surface flaw which might allow stable crack growth on loading to occur for that geometry.

2.2 Single Cycle Proof Testing Strategy

The philosophy underlying single cycle proof testing is well established; for example, see the work of Tiffany [5]. Perhaps the most well known example of the successful application of proof testing is that of the low temperature testing of the F-111 wing box at McClellan Air Force Base [6].

As a prelude to understanding multi-cycle proof testing, let us first consider the basic concept of single cycle proof testing of a material under brittle conditions. This can best be accomplished by examining Figure 1 which illustrates conventional proof testing logic in terms of both the residual strength (σ_r) and the residual fatigue life (N_f) of a structural component. As indicated, the proof test stress (σ_p) is selected to be some fraction of the material's ultimate strength (σ_{ult}) such that gross deformation of the structure is avoided, although local yielding may occur at geometric stress concentrations, or where large cracks have significantly reduced the net section in a given region. Since brittle materials exhibit a well-defined instability point given by $K_{max} = K_{Ic}$, the successful application of σ_p guarantees that any flaw that may be present is less than some size, a_i. Using a_i as the initial crack size in a fracture mechanics based fatigue crack growth analysis defines a corresponding initial residual fatigue life, N_i. Provided periodic proof testing can reliably ensure that the maximum crack size remains below a_i, in-service proof testing offers the opportunity to extend the life of the component. The interval (a_f - a_i) defines the crack size regime over which periodic proof testing at σ_p will result in crack detection through proof failures, thereby removing the component from service before the critical flaw size, a_f, is reached.

Although the foregoing discussion uses the term "brittle material", it is important to recognize that whether or not a material exhibits brittle behavior is dependent upon geometric constraint and loading rate, as well as test temperature. In fact, the temperature dependence of the material can be used to advantage in designing the proof test. Specifically, for materials in which K_{Ic}/σ_{ys} is significantly reduced as temperature is decreased, σ_p/σ_{ys} can be reduced

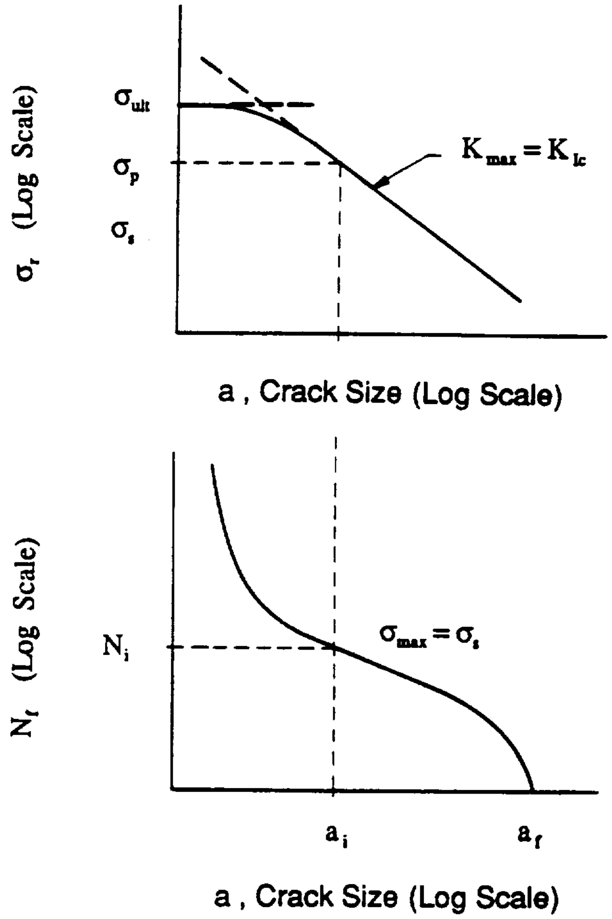

σ_r = Residual Strength

σ_{ult} = Ultimate Strength

σ_p = Proof Stress

σ_s = Service Stress

N_f = Residual Fatigue Life

N_i = Residual Fatigue Life Corresponding to a_i

a_i = Upper-Bound Initial Crack Size Determined by Proof Test

a_f = Final Crack Size at Instability

$a_f - a_i$ = Crack Growth Interval Available for Crack Detection

FIGURE 1. Single-cycle proof stress logic represented in terms of residual strength and residual fatigue life.

by performing the proof test at a temperature lower than the operating temperature. This strategy was used in the case of the F-111 proof testing [6], and more recently in the case of cryogenic proof testing of titanium disks in the Air Force's F-100 engines in F-15 and F-16 fighter aircraft.

2.3 Multi-Cycle Proof Testing and the R-Curve Concept

There is no advantage to multi-cycle proof testing in materials which behave in a brittle fashion, since significant stable crack growth on loading does not occur. However, multi-cycle proof testing appears to offer distinct advantages in materials which behave in ductile fashion, as demonstrated by Rocketdyne's experiences summarized in the previous section. The apparent success of multi-cycle proof testing is believed to be due to the occurrence of stable crack growth on loading. In general, this phenomenon is dependent on a variety of factors--including stress state, temperature and material condition-- and can best be understood in terms of resistance curve concepts.

The general concept of a resistance curve is attributable to Krafft [7] and involves an energy balance between the driving force for crack growth and the inherent resistance to crack growth of the material. Subsequently, McCabe and co-workers (e.g., see Ref. [8]) popularized the approach and developed standard methods for measuring R-Curves under linear elastic conditions. The approach has also been shown to apply to cyclic loading [9,10]; thus, its use is compatible with a conventional fracture mechanics approach to fatigue crack growth. More recently, the resistance curve concept has been extended to fracture under elastic-plastic loading [11,12] using the J-integral [13]. The latter has been formalized by Paris and co-workers [14,15] into the tearing instability approach. Thus, the resistance curve is a useful engineering concept which is applicable to a variety of failure modes and loading conditions, including stable crack growth within highly deformed regions at geometric stress concentrations [16]. However, for simplicity, the following discussion relating resistance curve concepts and multi-cycle proof testing is presented within the framework of linear elastic fracture mechanics. Elastic-plastic loading is considered in the detailed model developed in Section 3.

As illustrated in Figure 2, the resistance curve concept can best be understood by considering both the driving force (K) and material resistance (R)* as functions of the extent of stable crack growth, Δa, which occurs during loading. Here the resistance curve, or R-curve, is compared for two materials: the brittle material exhibits a relatively flat R-curve (R_B), while that for the ductile material (R_D) rises steeply as the crack extends. The marked increase in the R-curve in the latter case is believed to be associated with the formation of shear lips near the surface of the specimen, reflecting the influence of a relative change in crack-tip stress state from plane strain to plane stress as the specimen surface is approached. The dashed lines emanating from a common point are the superimposed driving forces for increasing values of applied nominal stress σ_1 through σ_4. Although stable crack growth can occur when $K = R$, the onset of crack instability does not occur until both: $K = R$ and $\partial K/\partial a = \partial R/\partial a$. Because of the flatness of the R-curve in the case of the brittle material,

---

* Under linear elastic loading, the materials resistance is also commonly referred to as K_R, but R will be used here for clarity.

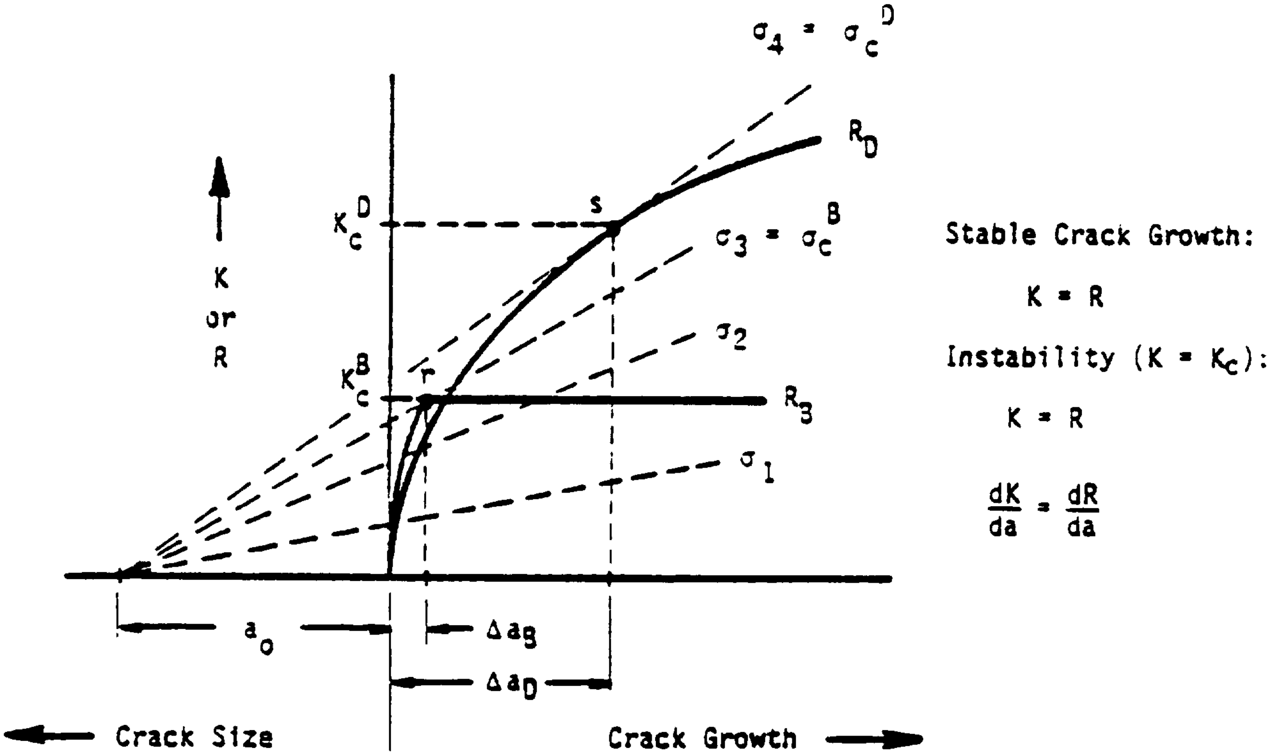

Stable Crack Growth:

$K = R$

Instability ($K = K_c$):

$K = R$

$$\frac{dK}{da} = \frac{dR}{da}$$

FIGURE 2. Influence of R-curve on maximum extent of stable crack growth in "Brittle" ('B') versus "Ductile" ('D') materials.

these conditions can only be met at point *r*, for an applied stress σ_3. Thus, σ_3 is a critical stress, designated σ_c, and provided the extent of prior crack growth (Δa_B) is small, this corresponds to K_{Ic}.

In contrast, for the case of ductile materials, instability occurs at point s, corresponding to a critical stress σ_c^D, and toughness K_c^D. As a consequence of differences in the nature of the *R*-curve, both the toughness and the extent of crack extension prior to instability can differ significantly. Moreover, contrary to the case of the brittle material, the value of apparent toughness for the ductile material is not unique, as will be discussed below.

For example, Figure 3 schematically shows how the character of the R-curve changes as a function of specimen (or component) thickness. Consequently, even for a fixed material, specimen geometry, and initial crack size, the toughness is seen to systematically increase with decreasing thickness, B. Moreover, altering the planar geometry such that the applied K varies, as shown in Figure 4, causes the toughness and extent of stable crack growth (Δa_1 versus Δa_2) to change significantly, even though the material and initial crack size are held constant. Finally, even for a constant planar geometry, thickness, and material, the apparent toughness (K_c) can vary with initial crack size as a result of crack resistance development during stable crack growth, as shown in Figure 5.

It follows from the above conditions that brittle materials have a straightforward proof test logic, as summarized previously in Figure 1. In contrast, the propensity for stable crack growth and more complex instability conditions of ductile materials give rise to the less certain proof test logic of Figure 6. Here stable crack growth on loading (Δa), due to the *R*-curve effect, produces uncertainty in the residual strength ($\delta\sigma_r$), as well as in the residual fatigue life (δN_f).

In theory the above uncertainty can be eliminated through the proper application of *R*-Curve concepts [1,3], although this has not yet been demonstrated quantitatively, nor have the relevant *R*-curve data been generated, especially for surface and embedded defects.

Based on the above discussion, it is clear that the character of the material's resistance curve is important to MCPT behavior and holds the key to proper selection of an optimum proof test strategy. Materials which are either inherently tough (Figure 2), or are used in thin sections (Figure 3), are candidates for multi-cycle proof testing. Conversely, materials with inherently low toughness, or those subjected to high degrees of geometric constraint, are candidates for single-cycle proof testing. Since Inconel 718, the primary structural material in the SSME, exhibits high toughness, it appears that component thickness and flaw geometry would be the primary geometric variables influencing the development of an optimum proof test strategy. This view is supported by Rocketdyne's five-cycle proof testing experience.

2.4 Potential Crack Growth Processes During MCPT

Crack growth can occur by several different mechanisms during a series of load-unload cycles, as follows: 1) rupture mechanisms such as brittle cleavage or ductile tearing; 2) true fatigue mechanisms associated with striation formation; and 3) interactions between rupture and fatigue. Here we will consider only elastic-plastic (ductile) fracture conditions.

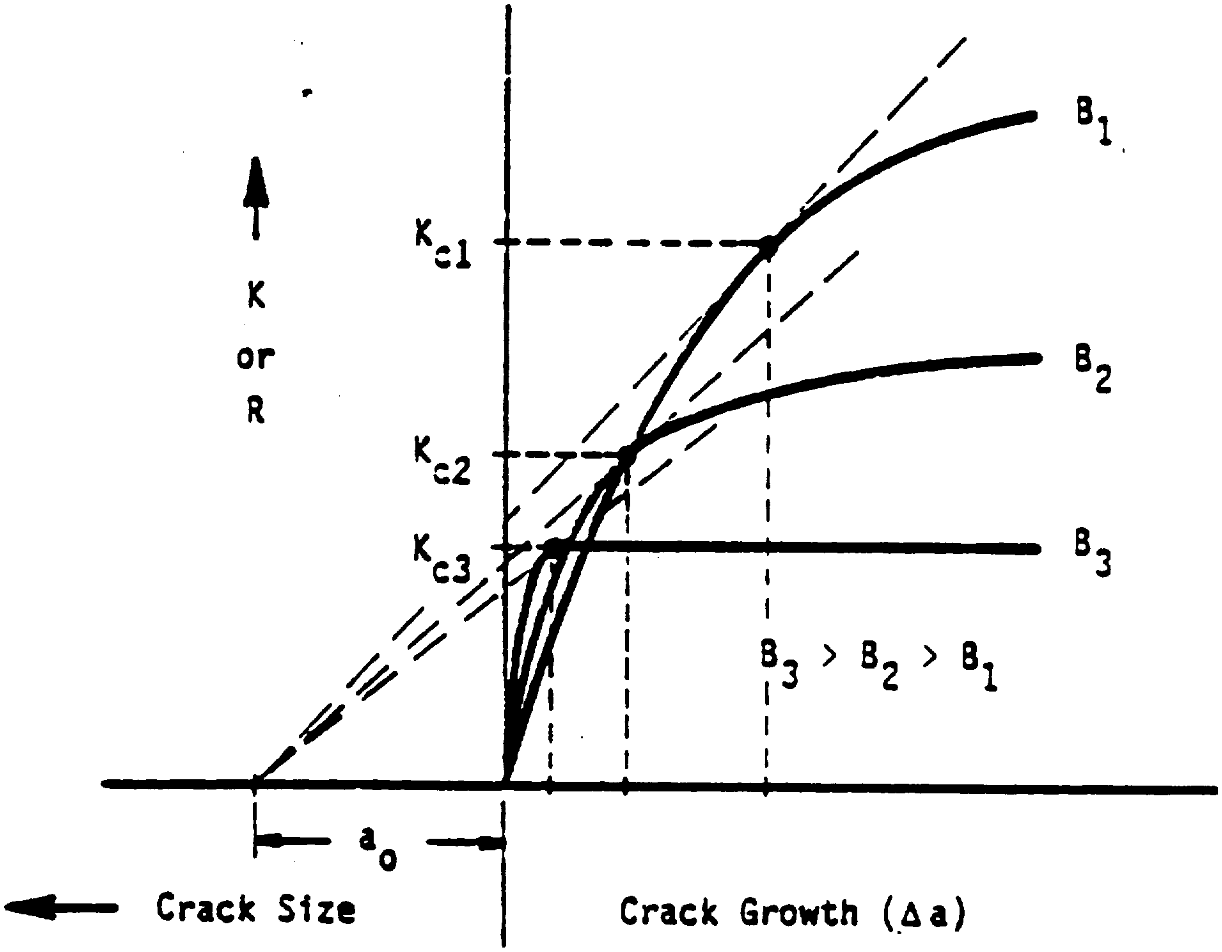

FIGURE 3. Influence of component thickness (B) on fracture toughness (K_c) and extent of crack growth (Δa) for a given material condition and initial crack size (a_o).

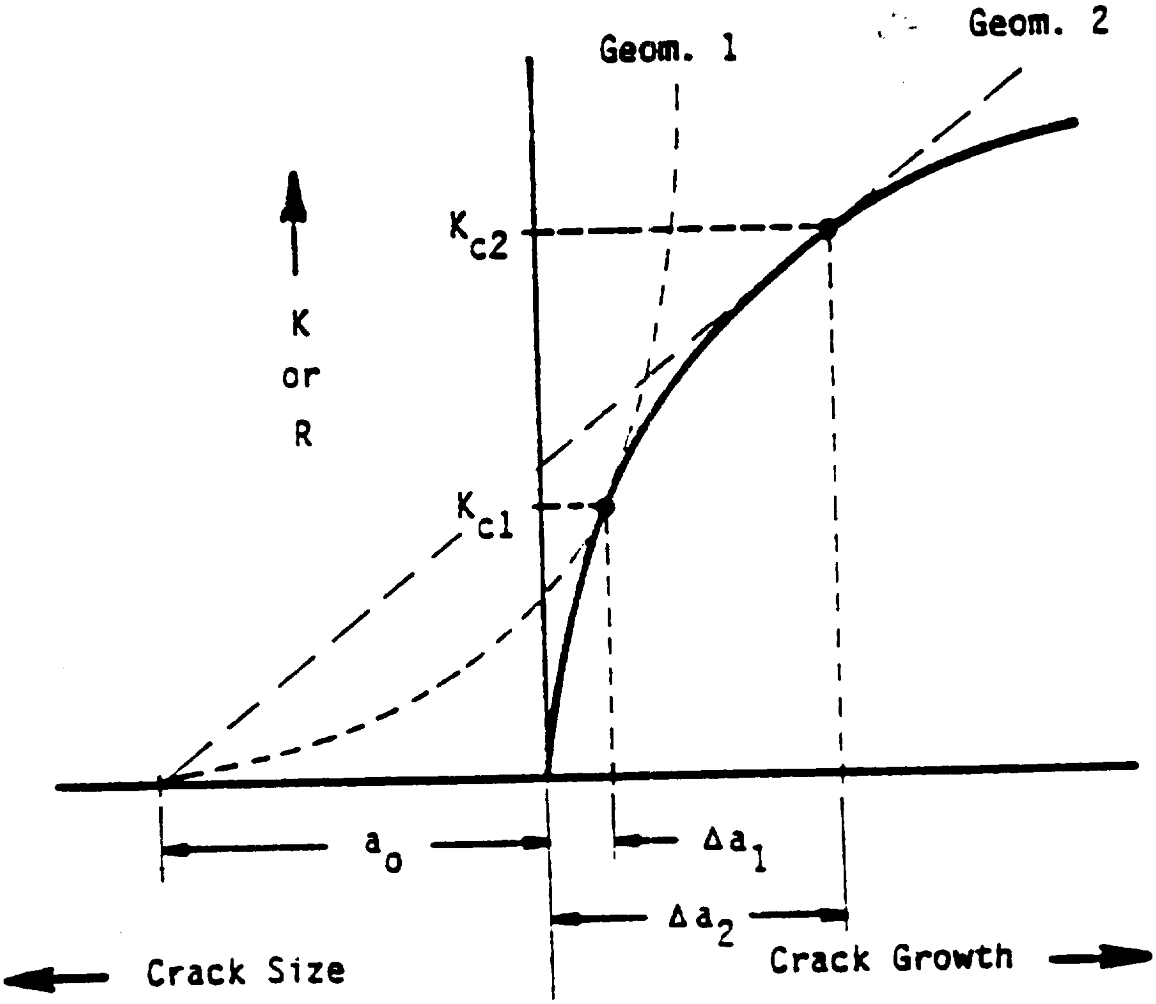

FIGURE 4. Influence of component geometry on the fracture toughness (K_c) and extent of crack growth (Δa) for a given material and initial crack size (a_o).

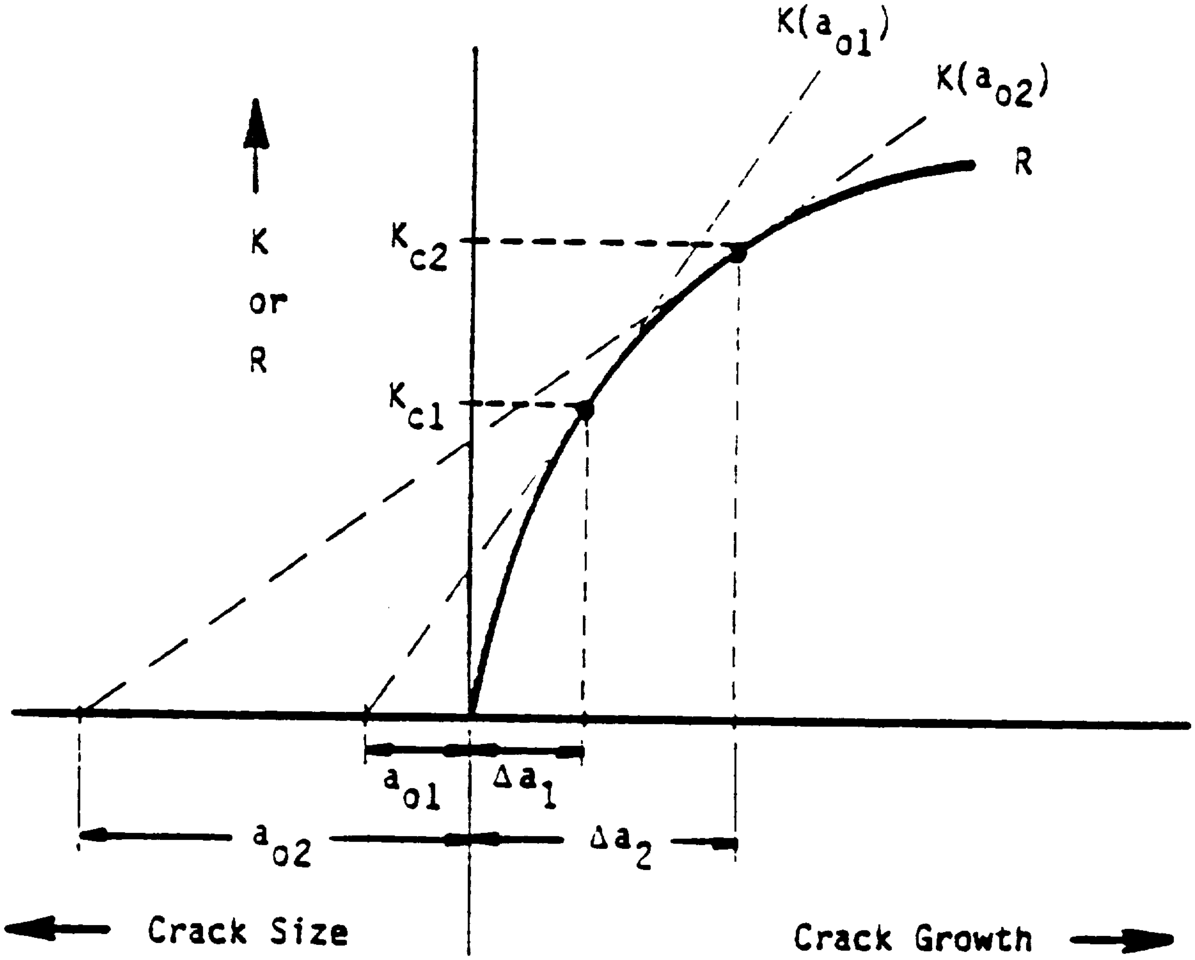

FIGURE 5. Influence of initial crack size (a_o) on the fracture toughness (K_c) and extent of crack growth (Δa) for a given material and geometry.

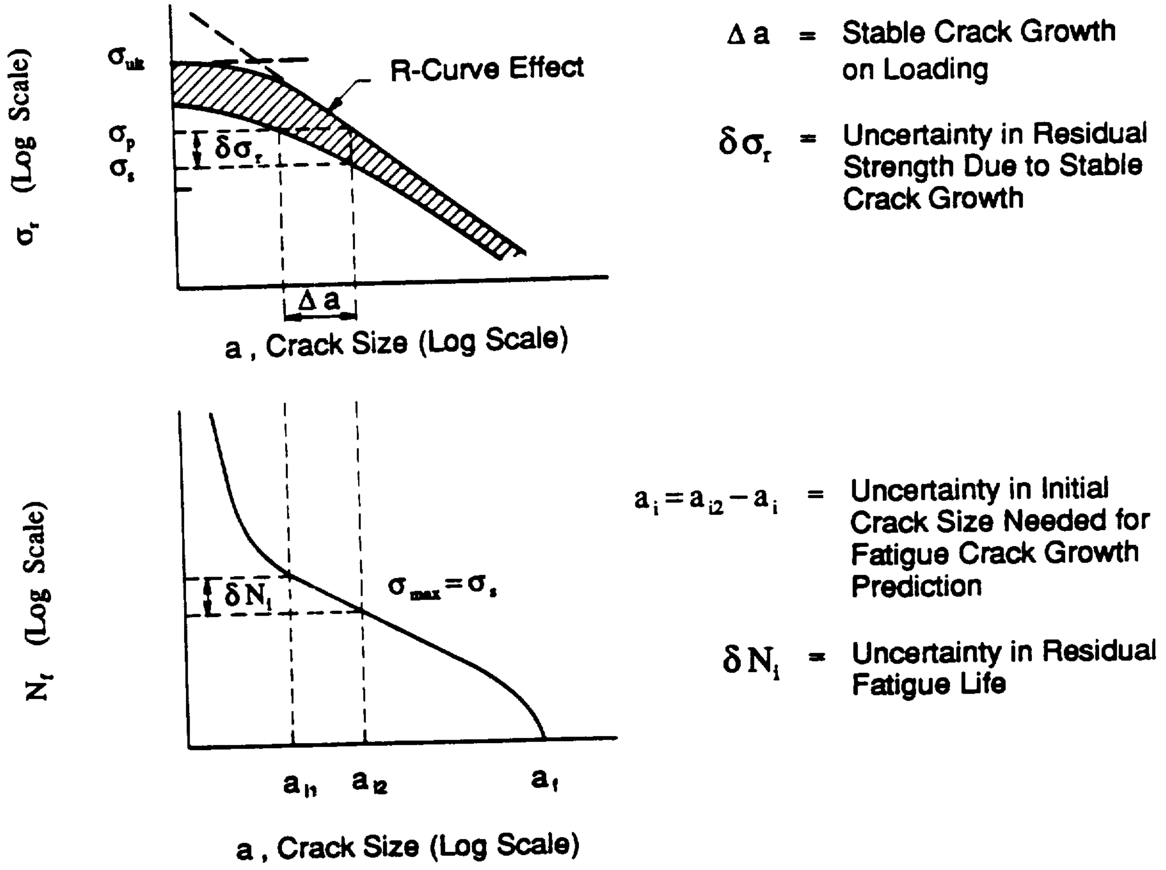

FIGURE 6. Uncertainty in residual strength and residual fatigue life due to stable crack growth on loading during the proof test of "ductile" materials.

2.4.1 Crack Growth by Ductile Tearing

Traditional ductile fracture experiments, and corresponding analyses, have been developed to describe crack growth under monotonically increasing load or displacement. It is unclear what happens upon unloading and then reloading during a period of ductile tearing. Two extreme behaviors are possible, as well as a continuous range of intermediate behaviors between these extremes.

At one extreme (call this Type A behavior), if the unloading does not cause significant reversed plastic flow near the crack tip, the subsequent reload will be essentially elastic. In this case, the unload/reload cycle will cause no further crack growth (assuming that the reload is up to but not beyond the previous maximum load or displacement). An example of this behavior is given by the partial (perhaps 10%) unload/reload excursions used in single specimen J-R curve testing as a means of measuring elastic specimen compliance and hence determining the crack length [17]. These unload/reload cycles are specifically designed to have no effect on ongoing ductile tearing. If this behavior describes the crack during a multi-cycle proof test, then no crack growth (by ductile tearing) would occur at all on any proof cycle after the first. Several authors have reported Type A behavior [18,19,20].

At the other extreme (call this Type B behavior), the unloading can cause significant reversed plastic flow near the crack tip. In this case, the crack and the near-tip stress-strain field are essentially "reset" and the subsequent reload cycle can be treated as if it were the first loading cycle in a brand new test, where the present crack length is now taken as the final crack length from the end of the previous cycle. In this case, there can be appreciable crack growth on subsequent proof cycles, even if the maximum applied load or displacement is the same. While Type B behavior has not previously been analyzed in precisely this way, there is clear evidence in the literature of unloading effects which contribute to significant crack extension on subsequent reload cycles. Brust *et al.* [21], for example, report experiments and corresponding analysis using near-tip path-independent integrals for two steels. They found re-initiation during reloading at roughly one-half of the load prior to unloading (this was similar to the load level for initiation on the first loading cycle) and attributed the effect to reversed plastic flow near the crack tip during unloading. Marschall and Wilkowski [18] have also reported unload-reload tests with significant crack growth during reloading. On the other hand, it must be noted that Brust [22] has very recently observed Type A behavior in a similar numerical analysis of cracked 304 stainless steel (with no explanation yet forwarded), and as noted in the previous paragraph, Marschall and Wilkowski have observed Type A behavior many times as well.

At the present time there is no simple criterion to determine which type of behavior will occur during unload/reload cycles or where along the continuum between the two extremes the behavior is best described. It seems clear that the extent of the unloading will be a major factor in determining the subsequent response: if the unload is only small and the minimum load after the unload is still a large percentage of the previous maximum load, then Type A behavior will occur; if the unload is extensive, especially to a large compressive load, then Type B behavior seems likely. Thus, the nature of the boundary conditions, and the stiffness of the loading system, will also have some effect. Specifically, displacement-controlled situations which reverse back to zero displacement typically cause compressive reversed loads, while load control situations which reverse back to zero load may leave a considerable unreversed plastic deformation (and of course there are intermediate cases as well).

2.4.2 Crack Growth by Fatigue

On the other hand, crack growth can occur not by ductile tearing mechanisms but by fatigue mechanisms associated with the load cycling. This is particularly the case when the maximum applied load or displacement is relatively small, so that no tearing or cleavage is initiated, and the number of load cycles is large; this is simply the classical fatigue crack growth problem. But fatigue crack growth can also occur simultaneously with ductile tearing. Again, this is generally most significant when the number of load/unload cycles is large. A first estimate of crack extension attributable to fatigue mechanisms can be made with the usual Paris Law representation of growth rates:

$$\frac{da}{dN} = C(\Delta K)^m \tag{1}$$

where the empirical crack growth constants C and m are obtained from baseline tests under linear elastic conditions. In the case of fatigue contributions to crack growth during ductile tearing, considerable plastic deformation will be occurring and the linear elastic fracture mechanics parameter K would cease to be meaningful. What is meaningful, at least in an operational engineering sense, is the range of the elastic-plastic fracture mechanics parameter J. Employing the relationship between K and J,

$$J = \frac{K^2}{E'} \tag{2}$$

where $E' = E$ for plane stress and $E' = E/(1 - \nu^2)$ for plane strain, it is possible to compute an equivalent ΔK value from ΔJ and use an extrapolation of the LEFM crack growth data to predict an elastic-plastic fatigue crack growth rate. Several examples are available in the literature in which linear elastic and elastic-plastic fatigue crack growth rate data were jointly correlated by this type of analysis, including special attention to crack closure [23,24].

2.4.3 Combined Tearing and Fatigue Crack Growth

In practice, crack growth during large load/unload/reload cycles can occur simultaneously by both tearing and fatigue mechanisms. One estimate of the total crack extension can be made by simply summing the two independent contributions [25]:

$$(da)_{total} = (da)_{tearing} + \left(\frac{da}{dN}\right)_{fatigue} \Delta N \tag{3}$$

This approach is typically used in conjunction with the assumption of Type A tearing behavior. This implies that no further crack growth by ductile tearing occurs upon reloading until the previous maximum load or displacement is exceeded (or until extensive fatigue crack growth has occurred). The ductile tearing that does occur is estimated by analyzing the load-displacement behavior while totally neglecting the unload/reload cycle. This approach further assumes that there is no true interaction between tearing and fatigue.

Another approach to a combined analysis of tearing and fatigue is to modify the fatigue crack growth equation. The traditional Paris Law equation given above assumes a simple power law relation between the applied stress intensity factor range (or its elastic-plastic equivalent) and the crack growth rate. In other words, the logarithm of the crack growth rate increases linearly with the logarithm of ΔK. In practice, however, it has often been observed (for more brittle or more highly constrained materials) that when K_{max} approaches K_{Ic}, the crack growth rate can increase sharply. This has led to development of alternative crack growth laws such as the Forman Equation [26],

$$\frac{da}{dN}=\frac{C(\Delta K)^{m}}{(1-R^{\sigma})K_{Ic}-\Delta K} \tag{4}$$

where R^{σ} is the cyclic stress ratio. For ductile materials with J as the controlling parameter, this type of equation is not easy to implement, because there is not a uniquely defined critical value of J for unstable fracture of a specimen or component. Nevertheless, analogous equations can be developed [27]. Kobayashi *et al.* [28] suggest that the fatigue crack growth rate will begin to increase sharply when J_{max} reaches J_{Ic}.

An alternative viewpoint about the relationship between ductile tearing and fatigue mechanisms assumes some equivalence in the two crack growth processes. Ratwani and Wilhem [9] suggested that a single full range resistance curve for 2024-T3 aluminum could be constructed to include both fatigue and fracture data. They considered only K-based parameters (K_R and K_{max}), and the validity of this concept for J-based elastic-plastic fracture analysis has not been confirmed.

3. ANALYTICAL MODEL FOR MCPT

3.1 Model Formulation

As discussed in Section 2.4, one of the key considerations in formulating a model for MCPT is how to represent the J-resistance curve for stable crack growth, as well as whether or not to include subcritical crack growth from fatigue.

If we assume that ductile tearing behavior during unload/reload cycles is of Type A, then we may have assumed *a priori* that multi-cycle proof testing is of no benefit. This assumption is inconsistent with Rocketdyne proof testing experience, which is summarized in Section 2.1. Furthermore, there appears to be sufficient evidence from the literature that Type B behavior is possible, at least to some degree. Calculations of crack growth based on Type B assumptions are expected to give an upper bound to the actual behavior. But this is a useful calculation, and so for the purposes of this initial simulation of MCPT we have assumed Type B ductile tearing behavior. The design and implementation of future experiments will provide an assessment of this assumption. This information may also provide the basis for developing more exact models, if necessary.

As discussed in the previous section, fatigue contributions to crack extension are also possible. Based on extrapolation of the small-scale yielding fatigue crack growth data for Inconel 718 (see Figure 27, Section 5.2), however, it appears that fatigue crack growth increments may be relatively small unless J_{max} values are into the tearing regime. For these larger J_{max} values, the J-resistance curve seems to be the preferred means of characterizing crack growth, especially in view of uncertainties about fatigue crack growth acceleration in this regime. In view of these reasons, the analysis described in this report focused exclusively on a J-R approach to crack extension. Such an approach also served to simplify the analytical scheme and to bring about at least a small reduction in the complexity of these preliminary assessments. The potential significance of fatigue crack growth to this problem will be examined in more detail in subsequent investigations.

Based on the above view of stable crack growth, a computer code was written which numerically simulates multi-cycle proof testing under a variety of conditions. The code, written in standard FORTRAN-77, was assembled and exercised on an Apollo workstation. Several specialized post-processing graphics routines were also developed.

The code essentially conducts quantitative comparisons of the material resistance curve and the applied J curve (J_{app}) by a suitable overlaying of the two curves. Appropriate logic is employed on each simulated proof cycle to locate the resistance curve relative to the initial crack length and to identify the intersection of the R-curve with the J_{app}-curve. The code checks for non-initiation or failure on that cycle and then (if necessary) calculates the extent of stable crack growth. The complex non-linear form of both curves requires the frequent use of iterative numerical schemes to invert equations or locate points of intersection, and therefore a high premium was placed on computational efficiency in developing the code.

The material resistance curve in the code can be quantified by any one of several simple models developed by Orange [29]. These are all empirical equations which have no direct physical basis, but which have been demonstrated to provide satisfactory fits to experimental data. Five different models are available in the code, and the user has the freedom to select the one which best describes his material-geometry system. These models include an exponential form,

$$J_R = (R + T\Delta a)[1 - \exp(-\Delta a/C)] \tag{5}$$

a hyperbolic form,

$$J_R = \frac{(R + T\Delta a)\Delta a}{C + \Delta a} \tag{6}$$

an arctangent form,

$$J_R = (R + T\Delta a)(2/\pi)\arctan(\pi\Delta a/2C) \tag{7}$$

a hyperbolic tangent form,

$$J_R = (R + T\Delta a)\tanh(\Delta a/C) \tag{8}$$

and a power law form,

$$J_R = A_1(\Delta a)^{A_2} \tag{9}$$

In all of these equations, Δa is the increment of crack advance. In the first four equations, T represents the asymptotic slope of the tearing line, R the intercept of the tearing line with the $\Delta = 0$ axis, and C the Δ value on the asymptotic blunting line which corresponds to $J_R = R$. See Figure 7. In the power law equation, A_1 and A_2 are general empirical constants. The specific values of all these constants are dependent not only on the resistance data but also on the specific empirical equation chosen. The choice of a specific model, and specific model constants, involves a simple non-linear least squares regression of available experimental data. Independent of the model and constants chosen, the user also has the freedom to specify a value for J_{Ic}, the J value below which crack initiation (and therefore tearing) will not occur.

The J_{app} values are computed as a function of the material's constitutive properties, crack length and other specimen dimensions, and boundary condition -- either applied load or displacement. A different set of J_{app} equations is required for each specimen or component geometry. Equations for many cracked geometries are readily available in the Electric Power Research Institute (EPRI) elastic-plastic handbook [30], and estimation schemes are available for other geometries.

A key distinction is made between load-controlled and displacement-controlled configurations, and this difference has important implications for both the numerical calculation of J_{app} and the fundamental evaluation of multi-cycle proof testing. When the component or specimen is under pure load control with applied load P, J can be directly evaluated according to the general form:

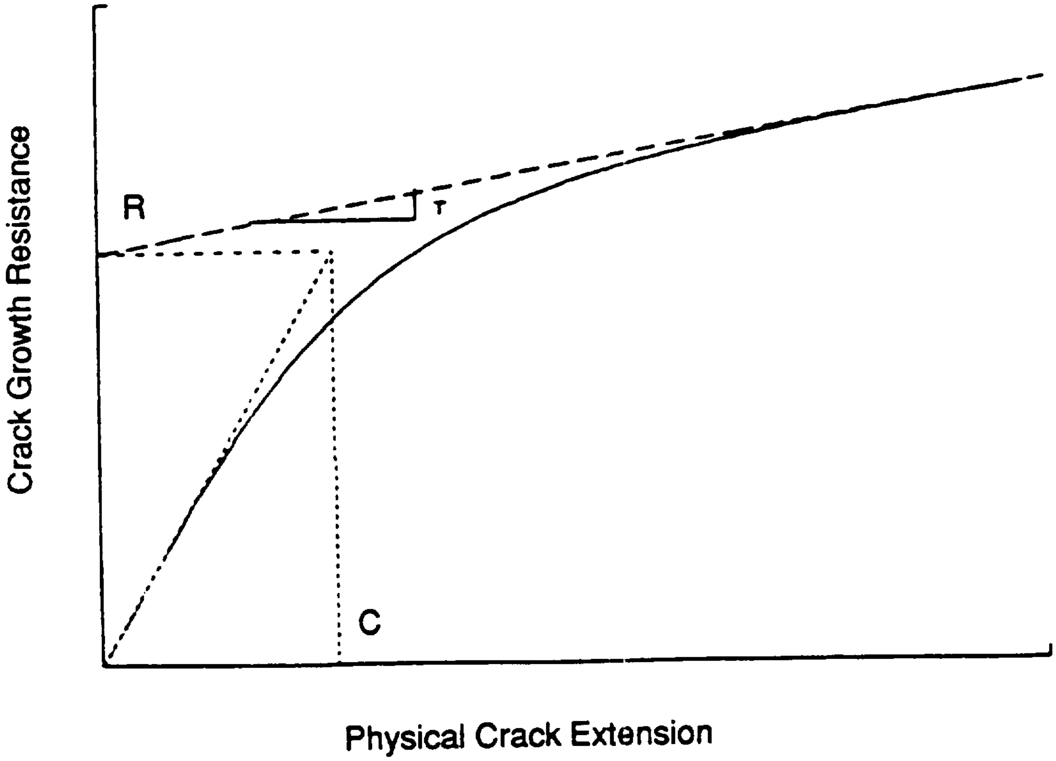

FIGURE 7. Schematic representation of elastic-plastic R-curves (adapted from Orange [29]).

$$J = F_1 P^2 + F_2 P^{n+1} \tag{10}$$

where F_1 and F_2 are known functions of specimen geometry, crack length, and material properties, and n is the strain-hardening exponent in a Ramberg-Osgood constitutive relationship. In this case, J increases monotonically with both load and crack length, sometimes quite sharply. When pure displacement control is applied with some total maximum displacement Δ, it is first necessary to determine the induced load by inverting a compliance equation of the general form:

$$\Delta = F_3 P + F_4 P^n \tag{11}$$

(where F_3 and F_4 are analogous but not identical to F_1 and F_2) and then substitute the calculated load into the previous equation in order to obtain J_{app}. Under pure (crack-mouth) displacement control, the J_{app} typically decreases with increasing crack length because of increases in the compliance, and corresponding decreases in the induced load.

In reality, many components and specimens are neither purely load-controlled or purely displacement-controlled, but exhibit some combination of load and displacement control. This may be described mathematically by assuming control based on total displacement Δ_T where

$$\Delta_T = \Delta + C_M P \tag{12}$$

Here C_M is the compliance of a linear spring placed in series with the cracked body and represents the elastic compliance of the total system. The condition $C_M = \infty$ corresponds to pure load control, and the condition $C_M = 0$ corresponds to pure displacement control. Intermediate values of C_M correspond to intermediate control configurations. For example, if a specimen is tested in displacement control with a very long gage length, the value of C_M may be related to the elastic compliance of the uncracked, load-bearing ends of the specimen between the crack and the gage point. Under combined control, the applied J value can either increase or decrease with crack length, depending on the choice of parameters in Eqs. 10 through 12. These different control conditions, and their influence on ductile crack growth during multi-cycle proof testing, will be illustrated and discussed in more detail in the following section.

The present computer code permits three different analysis schemes, each with appropriate graphical output. The first scheme simulates a single MCPT based on a single initial crack length and generates a complete graphical record of the J_{app} curve and the J-R curve, appropriately located for each proof cycle. The second scheme surveys a wide range of equally spaced initial crack lengths and identifies the corresponding final crack length after a given number of proof cycles, including the limiting crack lengths below which no growth occurs and above which catastrophic failure occurs during any of the proof cycles. The third scheme is a full Monte Carlo simulation which samples a given distribution of initial crack lengths and computes the corresponding distribution of final crack lengths. This scheme also admits the possibility of a statistically describable variation in any other input variable, such as changes in the J-R curve.

The heart of the computer code, including its many options, has been extensively validated by comparison to single-cycle fracture analyses given in the EPRI elastic-plastic fracture handbook [30]. Particular attention has been given to analysis of a compact-tension (CT) specimen of A533B steel under several different control conditions. Because this geometry-material system is well-understood and well-behaved, it also serves as a useful vehicle to illustrate many of the basic phenomena associated with MCPT.

3.2 MCPT Simulations with Thru-Thickness Cracks

3.2.1 MCPT Under Load Control Versus Displacement Control

A multi-cycle proof test for a CT specimen under pure load control is illustrated in Figure 8. The single J_{app} curve corresponds to the given maximum proof load, which is the same on each proof cycle. The five R-curves represent five different proof cycles, each curve emanating from the appropriate "initial" crack length at the beginning of the corresponding proof cycle. Each new "initial" crack length is determined by the intersection of the applied J curve with the resistance curve for the previous proof cycle. For example, the crack length at the beginning of the entire test is 4.615 inches. The intersection of the J_{app} curve with the R-curve originating at $a = 4.615$ identifies the amount of stable growth during the first proof cycle and therefore the crack length at the end of the first proof cycle, $a = 4.636$. This "final" crack length then serves as the "initial" crack length for the next proof cycle, identifying the new origin for the R-curve. In this particular multi-cycle proof test, failure occurs on the fifth proof cycle because for that initial crack length, the crack driving force exceeds the available material resistance, before the maximum proof load is attained, and $\partial J_{app}/\partial a > \partial J_R/\partial a$.

This specific example points out several general features of a load-controlled MCPT. First, note that the amount of crack growth is increasing with each additional proof cycle. Second, failure on the last proof cycle can occur at a load which is significantly lower than the proof load. Remember that the J_{app} curve shown is for the maximum load. Applied J curves for lower loads will lie below the curve shown. Failure will occur immediately above the load for which the J_{app} curve is just tangent to the last R-curve. Third, note that the extent of crack growth on each cycle and the number of proof cycles to failure will depend on a great many variables, including the proof load, the shape of the R-curve, and the initial crack length.

A MCPT under pure displacement control ($C_M = 0$) is shown in Figure 9. Here the J_{app} value decreases slowly and nearly linearly with crack length, and no failure occurs on any of the five proof cycles. This will be the general rule for any pure displacement control test: catastrophic fracture of the specimen or component will not occur, but the load-carrying capability of the structure may be seriously degraded.** The crack growth increments are successively smaller on each proof cycle, but in this case the total crack growth per cycle is relatively large, especially in comparison to the previous load-controlled MCPT simulation. The specific amount of crack growth during any load-controlled or

---

** In addition, it should also be noted that while this type of loading facilitates a leak-before-break condition, this situation may be catastrophic in components where an explosion of volatile fluids is likely.

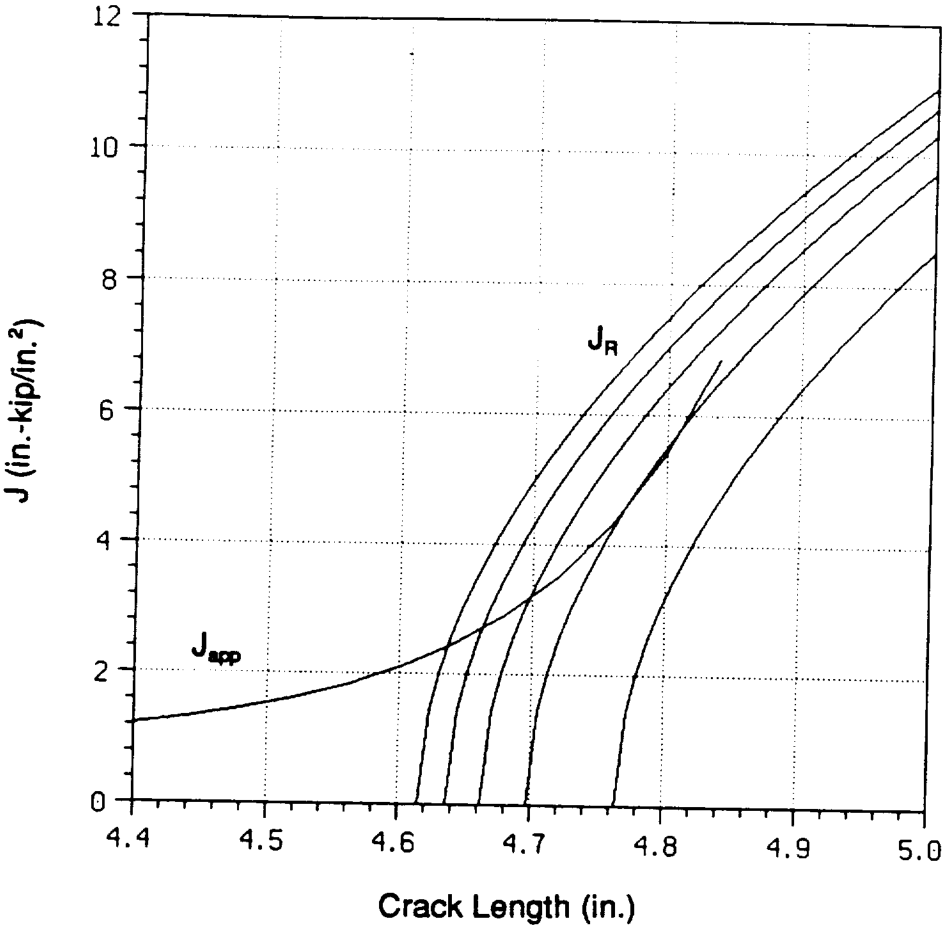

FIGURE 8. Example of a simulated multi-cycle proof test under load control.

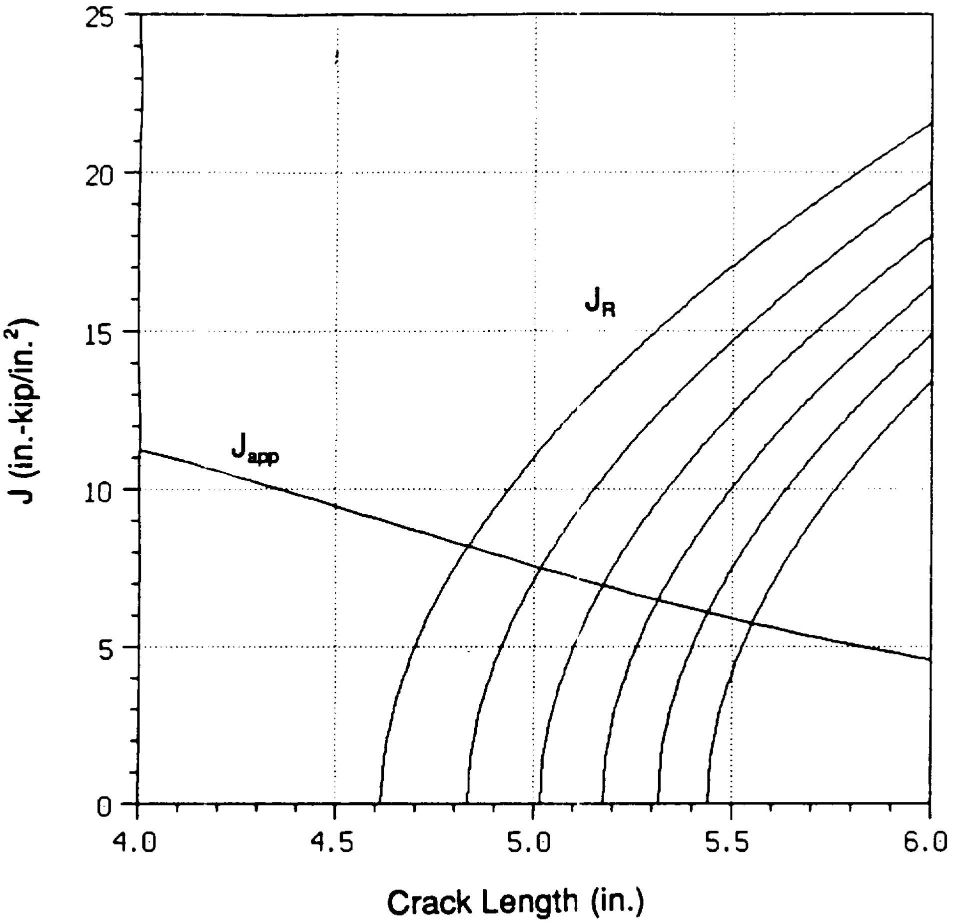

FIGURE 9. Example of a simulated multi-cycle proof test under displacement control.

displacement-controlled MCPT, of course, is a function of the specific applied loads or displacements. In general, however, displacement-controlled tests do possess a greater potential for extensive stable crack growth than load-controlled tests.

Intermediate control conditions can cause several different MCPT behaviors; two examples are shown in Figure 10. In the top figure, the J_{app} curve for the crack lengths of interest is similar to that for pure load control. However, the increase in J_{app} with crack length is less pronounced than for load control, and therefore the extent of stable crack growth is greater. Note that in this particular case, failure occurs on the fourth proof cycle. A very different type of MCPT phenomenon is illustrated in the bottom graph. For this particular case of intermediate control, the general character of the entire J_{app} curve is evident: a gradual increase in J with crack length to some maximum value, followed by a gradual decrease. (Actually, the J_{app} curve for pure displacement control exhibits both increasing and decreasing regions, but the increasing region is limited to very short crack lengths.) If the R curve intersects the J_{app} curve in the rising region, the MCPT behavior will be similar to a load control test, as in the top figure. If the R-curve intersects the J_{app} curve in the decreasing region, the MCPT will follow the general trends of a displacement control test. In this particular case, the MCPT encompasses both attributes of the J_{app} curve. With small variations in the initial crack length, applied displacement, or system compliance, a flawed structure of this type undergoing MCPT may fail during proof testing, experience large stable crack growth without any possibility of failure, or not even initiate a tearing crack. Thus, in theory the precise response to MCPT will be specific to component details.

3.2.2 Changes in Crack Size Distribution During MCPT

The effect of MCPT on a population of initial defects was evaluated using Monte Carlo simulation. The particular Monte Carlo scheme employed here has thus far only considered variations in the initial flaw size. All other input variables are taken as deterministic. It should be noted that other variables (such as the R-curve or the system compliance) also exhibit some randomness/uncertainty, and this may need to be considered in order to make a comprehensive evaluation of the MCPT scheme.

The Monte Carlo algorithm randomly selects an initial crack length from a user-defined probabilistic distribution. The code then conducts a simulated MCPT on this sample, noting whether the crack failed to begin tearing, grew to final fracture, or simply grew to some larger crack size. The code then collects all final crack lengths for the unfailed samples and displays frequency distributions for both initial and final crack lengths. The graphs presented here are not true probability distribution functions (PDF), but rather are histograms. The total range of crack lengths is divided into a large number of equally spaced bins, the actual crack lengths are sorted into the bins for counting, and then the graph is constructed by locating each bin total (the number of cracks in each bin range) at the crack length corresponding to the midpoint of each bin. This is a reasonable and efficient approximation of the true PDF, but may lack certain fine detail.

Typical results for a five-cycle proof test in intermediate control (tending towards load control) are shown in Figure 11. This figure may be better interpreted by referring to the schematic representation in Figure 12. Under these particular conditions, all cracks shorter than a_{th} do not initiate (J_{app} on the first cycle is less than J_{Ic}), and so all cracks in Region 1 remain unchanged in length throughout the MCPT. All cracks longer than a_{cr} will grow to failure on one of the five proof cycles, and hence none of the cracks

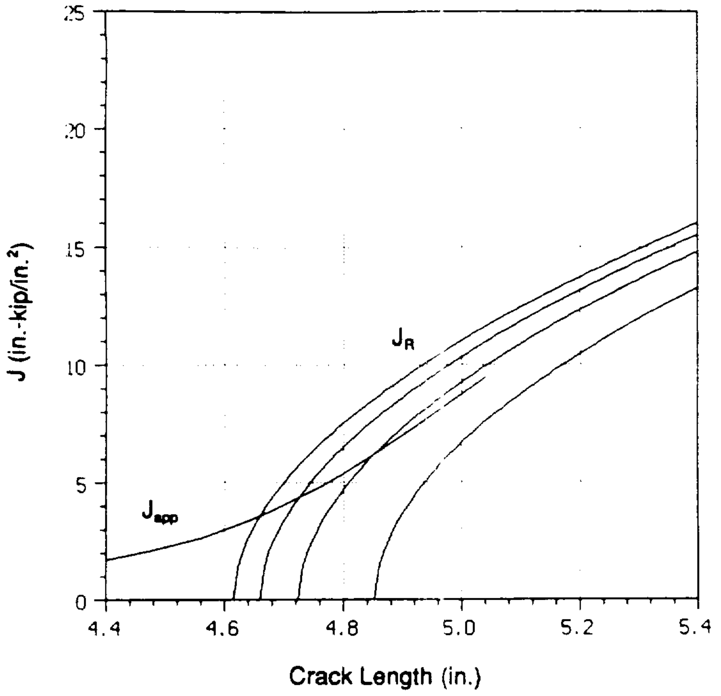

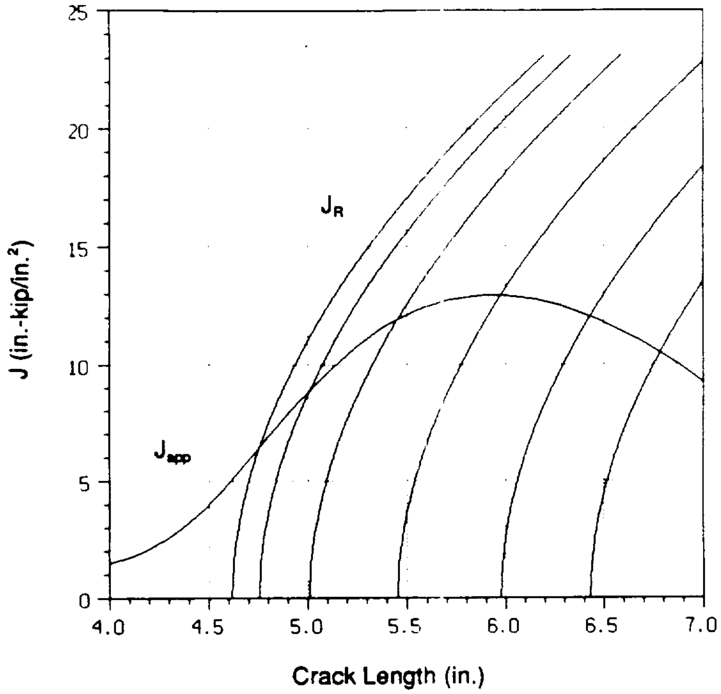

FIGURE 10. Examples of simulated multi-cycle proof tests under intermediate control.

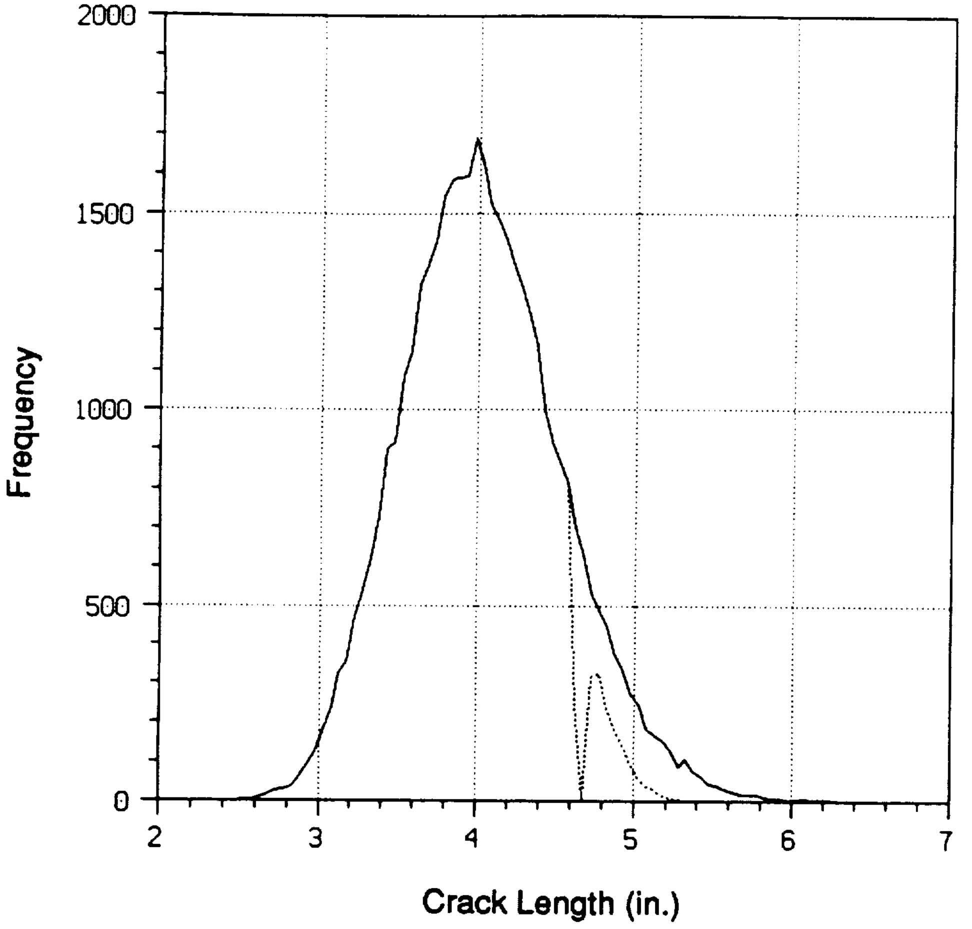

FIGURE 11. Initial (solid line) and final (dashed line) crack length distributions for simulated five cycle proof tests.

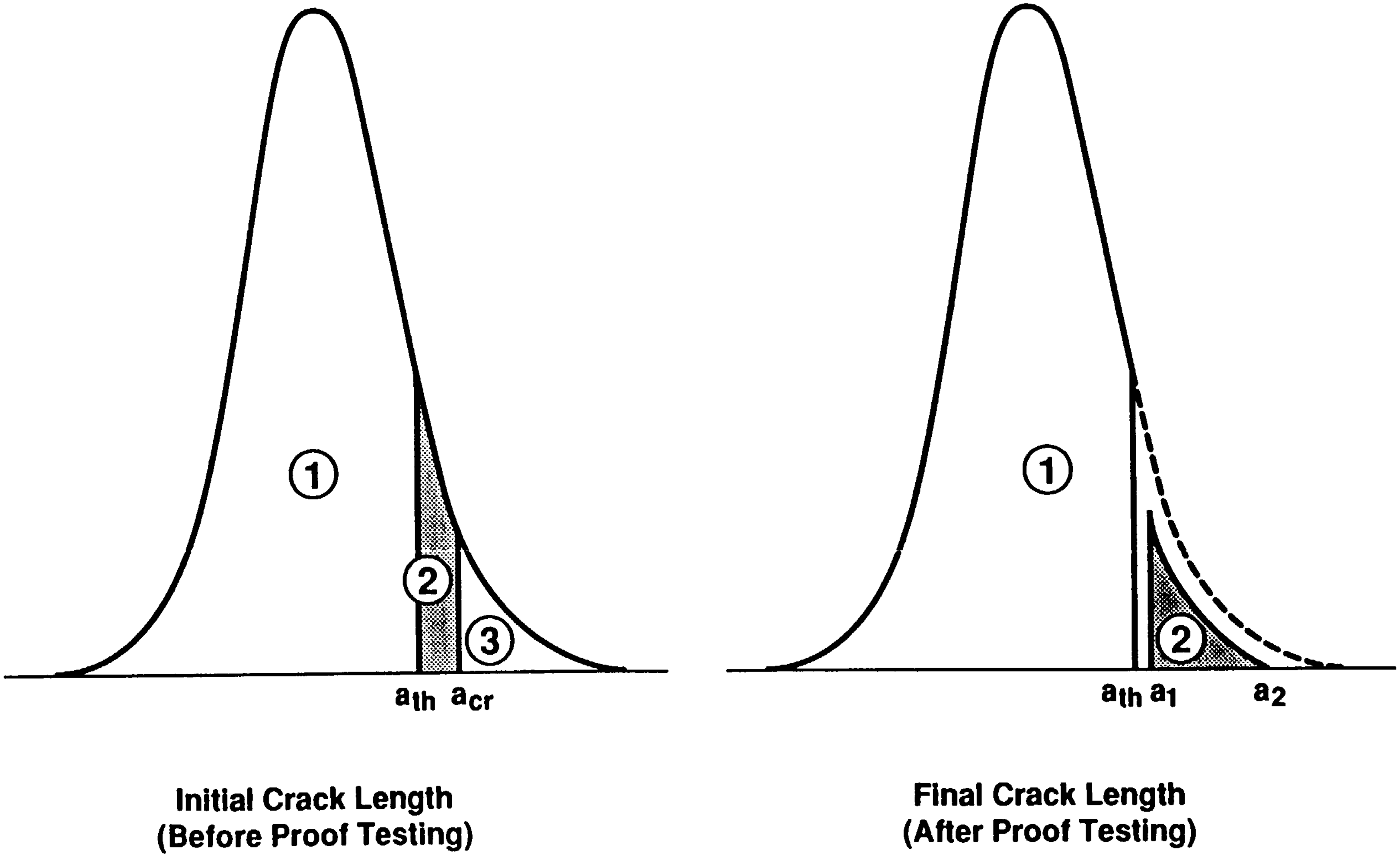

Initial Crack Length (Before Proof Testing)

Final Crack Length (After Proof Testing)

FIGURE 12. Schematic representation of initial and final crack length distributions for MCPT.

initially in Region 3 appear in the distribution of final crack lengths. The cracks in Region 2 will experience stable crack growth, but will not grow to fracture. The total areas of Region 2 in the initial and final flaw distributions are the same (i.e., both represent the same number of cracks). Note that there is actually a "gap" in the final flaw distribution (which in Figure 11 is partially obscured by the bin sorting operation) because flaws exactly equal to a_{th} are prevented from growing at all, while flaws slightly greater than a_{th} grow by some finite amount. This gap goes away as J_{Ic} approaches zero, but a non-zero J_{Ic} is supported by experimental evidence. Remember, also, that the present analysis considers only crack growth by ductile tearing and not by traditional fatigue, or sustained load mechanisms. This analysis assumes that cracks which never see a J greater than J_{Ic} will never grow, although a fatigue analysis would predict some (generally quite small in comparison) average crack advance on every cycle (if the fatigue threshold is exceeded).

Figure 13 illustrates MCPT results for the same conditions as Figure 11, but with different numbers of proof cycles. In this case, the advantage of multiple proof cycles is clearly evident. While the largest remaining crack length in the population does not change with further proof cycling, the population of cracks longer than a_{th} does decrease with larger numbers of proof cycles. The same general effect is evident in Figure 14, which uses initial flaw distribution types more typical of actual hardware (that is, log-normal distributions heavily skewed towards shorter flaws). In this case, by the end of 10 proof cycles almost all cracks longer than a_{th} have been removed from the population. On the other hand, it should be noted that in some cases very little benefit appears to be realized by further proof cycling beyond a single cycle. It should be obvious by now that a great many variables influence the outcome of MCPT, and it is not yet possible to suggest a simple rule of thumb about when MCPT is good or bad. Some general trends do, however, appear evident.

One such general trend is that MCPT under pure, or nearly pure, displacement control is not desirable. This fact is illustrated in a striking way in Figure 15. In this case, no cracks have been removed from the population but all cracks have experienced significant stable growth. The same conclusion would apply to intermediate control configurations where the R-curve intersects the J_{app} curve in the falling region as in Figure 10.

Monte Carlo simulation of MCPT for intermediate control cases has just begun (numerically this is quite complex because of the complex shapes of both J_{app} and R-curves, and the probability of multiple intersections), but it is obvious that several different outcomes are possible. Identification of the actual control boundary conditions in real components will be particularly crucial to the final evaluation of MCPT.

3.3 *J* Estimates for Surface Cracks

These numerical experiments have been conducted on reference geometries and materials in order to validate the code and illustrate the fundamental physical phenomena. The ultimate concern, however, is to make some judgements about specific flaw shapes, flaw sizes, material properties, and applied loads which are representative of SSME hardware. Unfortunately, some of these requirements add new uncertainties to the analysis and require further development work. Initial efforts to identify the governing equations and input properties which are specific to the SSME application are briefly described below.

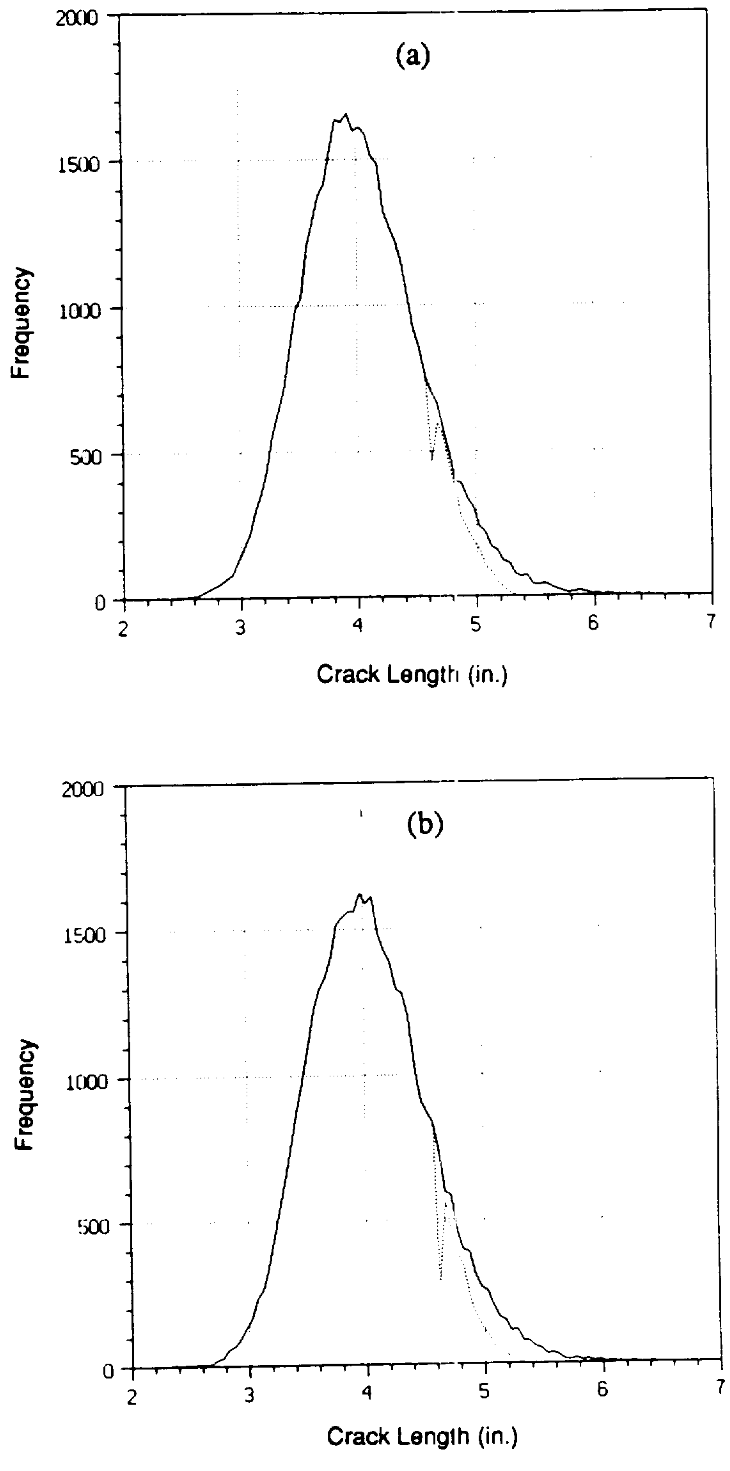

FIGURE 13. Initial and final crack length distributions for simulated proof tests with (a) one and (b) two proof cycles. Simulation parameters are otherwise the same as for the five-cycle proof test illustrated in Fig. 11.

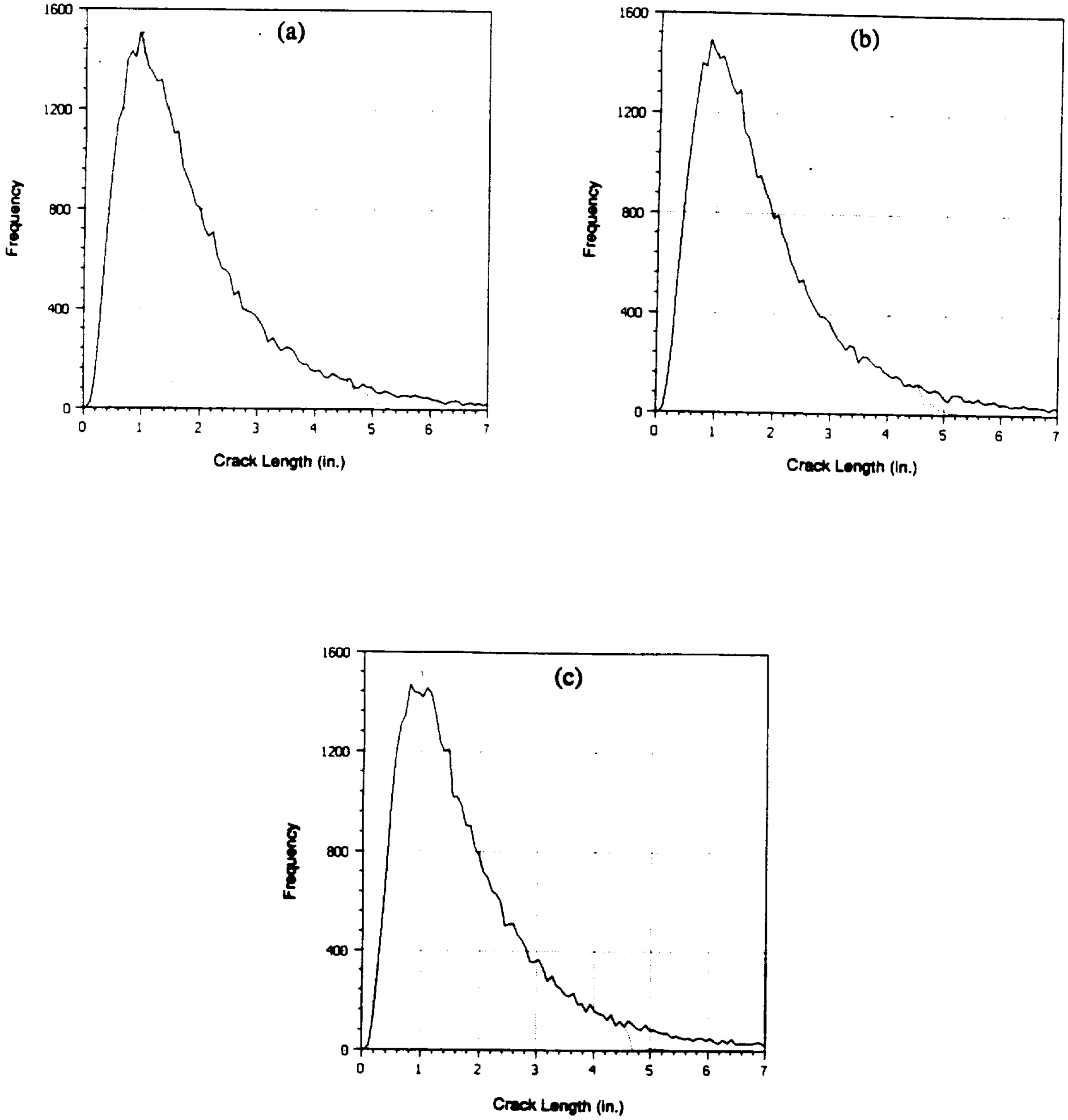

FIGURE 14. Initial (solid line) and final (dashed line) crack length distributions for simulated multi-cycle proof test schemes with different numbers of proof cycles.
(a) 1 cycle
(b) 5 cycles
(c) 10 cycles

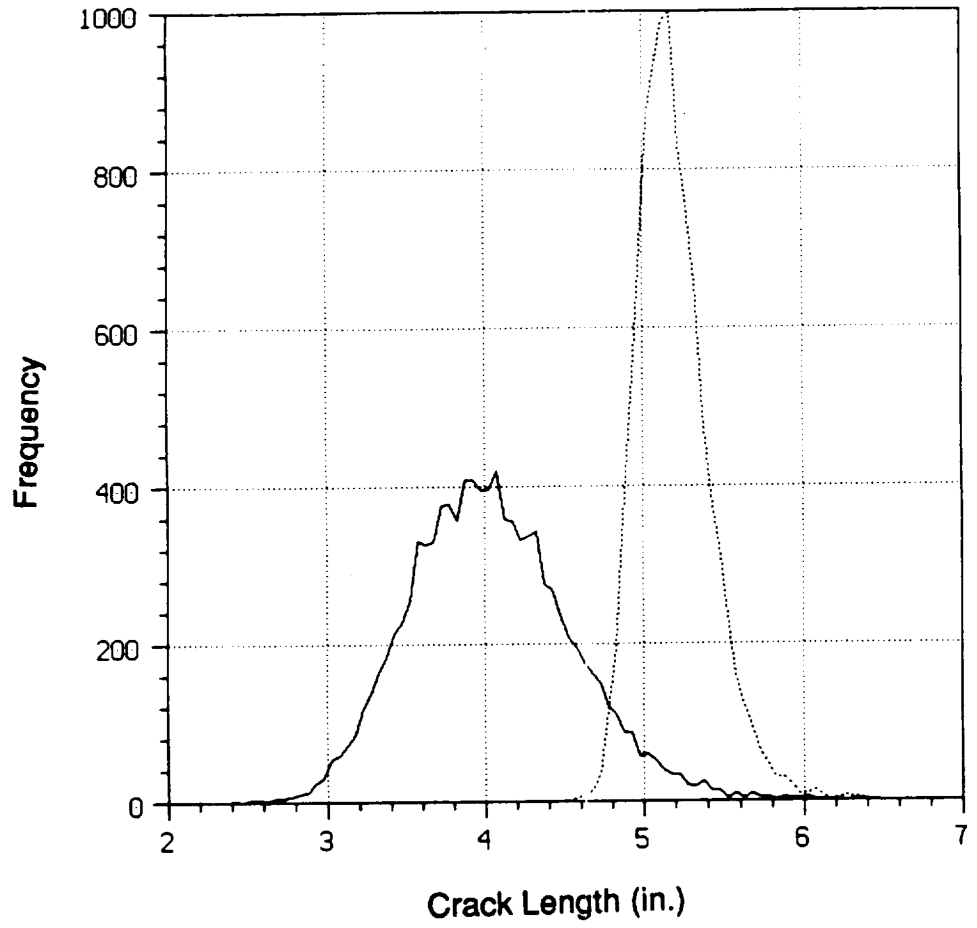

FIGURE 15. Initial (solid line) and final (dashed line) crack length distributions for an extreme example of simulated multi-cycle proof testing under pure displacement control.

J-integral estimation schemes for compact tension specimens, edge-cracked plates, and many other "standard" specimen geometries are immediately available in the EPRI elastic-plastic handbook. Closed-form estimates for surface or embedded cracks in finite thickness plates or shells are not readily available. A limited number of finite element results for specific crack and specimen geometries and materials have been published, but these have not yet led to generalized analytical expressions.

An alternative approach to J estimation is the reference stress approach developed by the Central Electricity Generating Board (CEGB) of the United Kingdom [31]. This technique requires only three basic pieces of information: 1) a complete solution for the linear elastic stress intensity factor K; 2) a description of the elastic-plastic constitutive material response (which does not have to be of the Ramberg-Osgood form); and 3) an estimate of the plastic collapse limit load for the cracked member, assuming an elastic-perfectly plastic material. All three of these are available for the surface cracked plate and the Inconel 718 material. A remaining ambiguity for the surface cracked plate is whether the limit load should represent the local limit load for break-through to the back surface or the global limit load for failure of the entire plate. Investigations by Miller of the CEGB [32] suggest that the global limit load provides better J estimates, and his comparisons of reference stress estimates with the limited number of "exact" solutions available at that time found the estimate to be acceptable.

We have made further comparisons of the reference stress estimates for surface cracks in finite thickness elastic-plastic plates with recent finite element results published by Parks and Wang [33]. These comparisons are summarized in Figure 16, where J is normalized by $\sigma_0\varepsilon_0 t$ and the applied stress is normalized as σ_∞/σ_0. The material constants σ_0 and ε_0 are based on a Ramberg-Osgood description of the elastic-plastic constitutive relationship (which was used by Parks and Wang),

$$\frac{\varepsilon}{\varepsilon_0}=\frac{\sigma}{\sigma_0}+\alpha\left(\frac{\sigma}{\sigma_0}\right)^n \qquad (13)$$

The general form of the reference stress estimate for J used here is given by the expression

$$J=K^2\frac{\varepsilon_{ref}}{\sigma_{ref}}\left\{1+\frac{1}{2}\left(\frac{\sigma_{ref}}{\sigma_{ys}}\right)^2\left(\frac{\sigma_{ref}}{E\varepsilon_{ref}}\right)^2\right\} \qquad (14)$$

This equation includes an effective crack length term to approximately account for plasticity in the intermediate small-scale yielding regime [34]. The reference stress for a surface-cracked plate is calculated as

$$\sigma_{ref}=\frac{\sigma_\infty}{1-(\pi a^2)/(2tw)} \qquad (15)$$

where t and w are the thickness and width of the specimen and σ_∞ is the nominal applied stress. The reference strain ε_{ref} is calculated from the constitutive relationship as the uniaxial

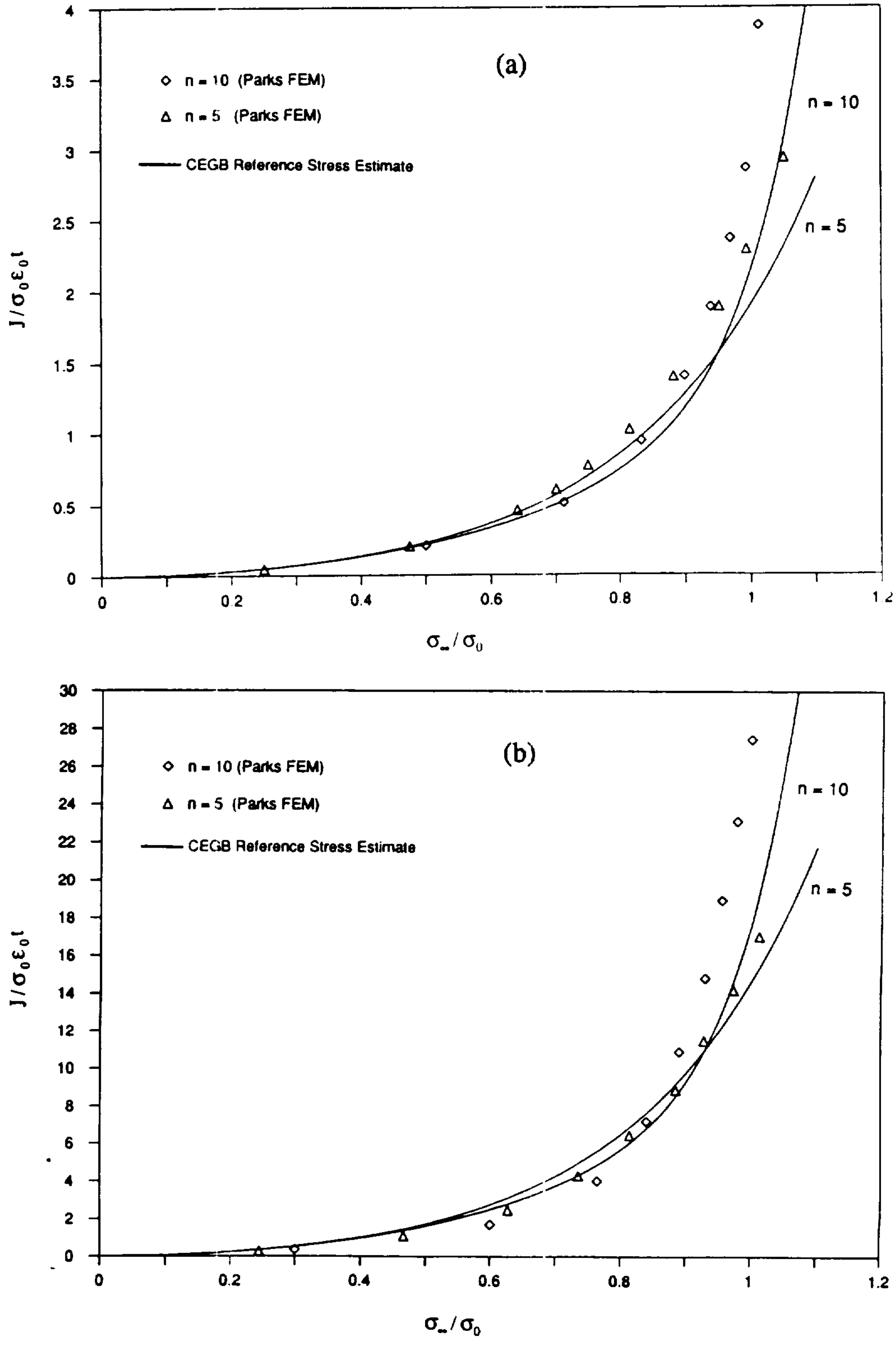

FIGURE 16. Comparison of reference stress method for J estimation with finite element results of Parks and Wang [33] for surface cracks in finite plates.
(a) semi-circular (a/c = 1, a/t = 0.5)
(b) semi-elliptical (a/c = 0.24, a/t = 0.6).

strain corresponding to σ_{ref}. The linear elastic stress intensity factor K is calculated from the expressions of Newman and Raju [35]. The reference stress J estimate appears to be significantly low for both crack shapes.

Dowling [36] has previously studied J estimates for semi-circular flaws in infinite bodies. He derived an equation of the general form

$$J = \frac{K^2}{E}{}'\left\{1 + \frac{J_z}{J_e} + h_0 \frac{E'}{E} \frac{\alpha(\sigma/\sigma_0)^n}{\sigma/\sigma_0}\right\} \tag{16}$$

Here J_z/J_e is an effective crack length (plastic zone) correction term and h_0 is a function of the strain hardening exponent. Dowling found an equation of this form to give very similar results to the elastic-plastic finite element analysis of Trantina et al. [37].

For infinite bodies, the reference stress is equal to the applied stress, and so we may rewrite the previous equation (for plane stress) as:

$$J = \frac{K^2}{E}\left\{1 + \frac{J_z}{J_e} + h_0\left(\frac{\varepsilon_{ref}E}{\sigma_{ref}} - 1\right)\right\} \tag{17}$$

Ignoring for the moment the effective crack length term J_z/J_e, this equation differs from the basic CEGB reference stress equation only by the h_0 factor, which the CEGB estimate for an infinite body would take to be equal to 1. An arbitrary modification to the reference stress J estimate can then be made by applying this last equation to the general case of a finite body, where the reference stress and strain will be higher than the nominal applied values. These new estimates are compared with the Parks and Wang results in Figure 17, and they are clearly much improved. These results are promising, although further study is needed to confirm this modified estimation procedure.

Consideration of displacement control or intermediate control configurations requires not only estimates for J as a function of load but also total displacement as a function of load and system compliance. Again, this is not readily available for the case of surface flaws. McCabe [38] has recently proposed equations (developed by Newman and Raju) for the elastic component of displacement, and he has also proposed an algorithm by which experimental results can be used to calibrate a plastic displacement relationship of general form. Further studies are underway to determine if SwRI data can be used to construct these equations.

3.4 MCPT Simulations with Surface Cracks

Preliminary assessments of multi-cycle proof testing for SSME applications were conducted using the computer code described above in Section 3.1. The necessary J estimation scheme for surface flaws was described in Section 3.3. Also required as input are information about initial crack size distributions, discussed in Section 4, and material properties and a resistance curve for surface flaws in IN-718, both of which are discussed in Section 5.4.

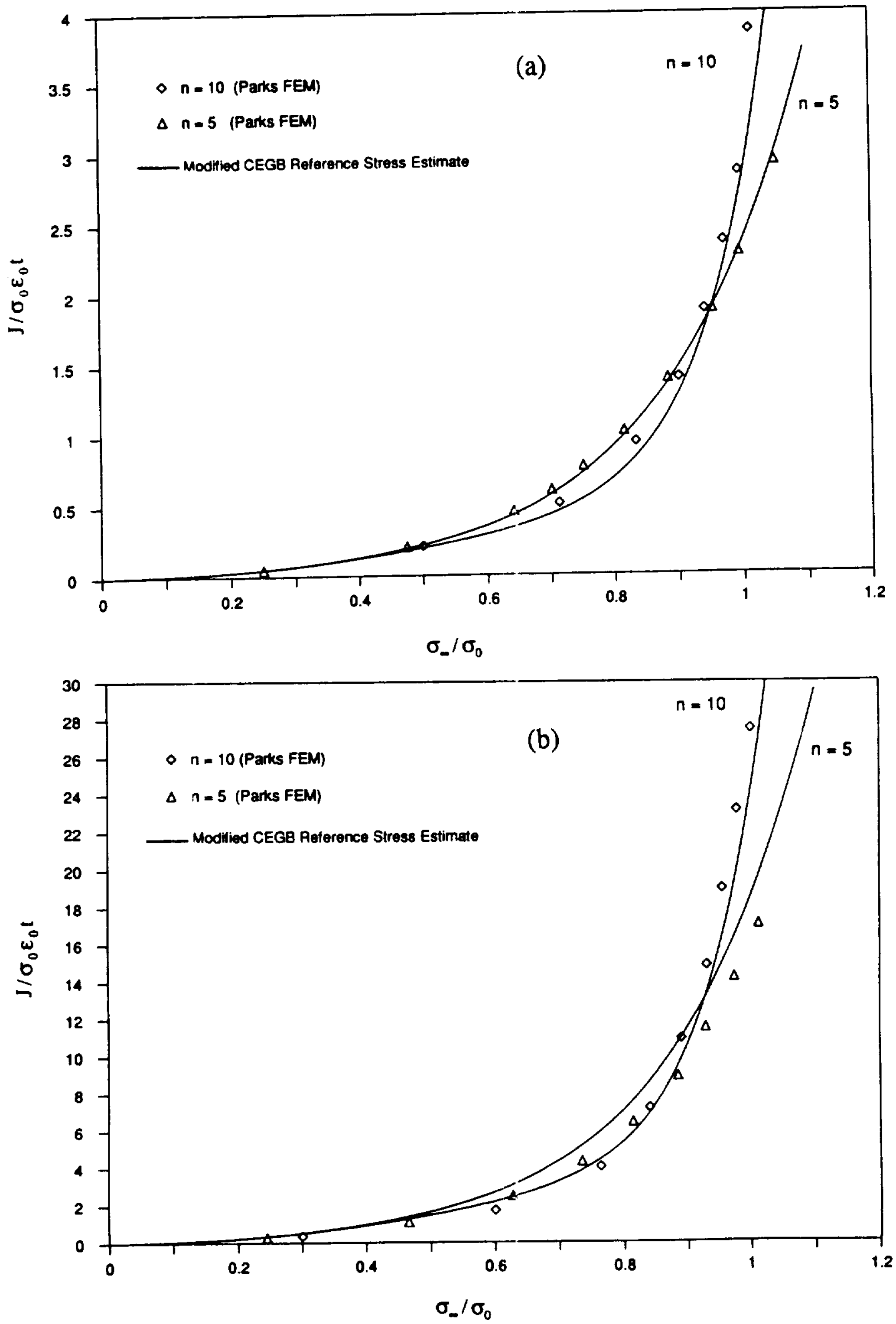

FIGURE 17. Comparison of modified reference stress method for J estimation with finite element results of Parks and Wang for surface cracks in finite plates.
(a) semi-circular (a/c = 1, a/t = 0.5)
(b) semi-elliptical (a/c = 0.24, a/t = 0.6).

Two different representations of the resistance curve were investigated. The development of the experimental data and empirical models for the R-curve is discussed in more detail in Section 5.4, and is only summarized briefly here. One surface crack R-curve model was chosen to have the same initial and tearing slopes as a resistance curve for IN-718 based on compact tension specimens, but with the intercept of the tearing line (parameter *R*, Figure 7) increased by 3x. The second representation was a unique power-law fit to the surface crack J - Δa data, with J estimates based on the modified reference stress technique. The original data and the two fitted curves are shown together with Figure 18.

A Monte Carlo simulation of multi-cycle proof testing for the surface crack configuration used by SwRI is illustrated in Figure 19. This particular simulation used the power-law *J-R* curve. The control parameter was maximum load and the proof stress was roughly equal to the flow stress (180 ksi). The section thickness was 0.2 in. Five proof cycles were applied. Most of the cracks in the initial distribution are small and in this case, those small cracks do not grow appreciably. The larger cracks do grow noticeably but the net change in the crack length distribution is relatively small. See Figure 20, for example, where simulations of individual proof tests are shown. When the initial crack length is 0.06 in., the crack length is predicted to increase by about 0.005 in. after five proof cycles. When the initial crack length is 0.08 in., about 0.020 in. of total crack growth is predicted.

For this particular test configuration, the crack lengths of greatest interest are well into the tail of the distribution. Further simulations were conducted which focused on these longer initial crack lengths, as shown in Figure 21. Note here that only the right-hand tail of the distribution is shown. The top graph shows initial and final crack length distributions for five cycle proof testing with the same parameters described above. Here it is clear that proof testing removes from the population only cracks longer than 0.112 in. The frequency of cracks longer than about 0.07 in. decreases slightly after MCPT, and the frequency of cracks shorter than 0.07 in. is essentially unchanged. Compare these results with the bottom graph, which shows initial and final distributions for single cycle proof testing. The frequency of cracks having lengths greater than 0.085 in. decreases somewhat, but the change is less than for five cycle proof testing. The final maximum crack length is unchanged. One might conclude in this particular case that MCPT is superior but only marginally so.

Further studies are needed to examine a wider range of input parameters which are relevant to SSME proof testing. Attention must be given to displacement-controlled configurations, the exact form of the resistance curve, and other representative values of initial crack sizes and shapes, section thickness, and applied load. The material appears to be of sufficient toughness, however, that only extremely large cracks (perhaps deeper than half the section thickness) will be removed from the population during proof testing at large applied stresses. Lower applied proof stresses leave much longer cracks in the structure after testing. An applied maximum stress of 170 ksi, for example, is predicted to leave a maximum flaw depth of 0.136 in. for a section thickness of 0.2 in. Applied stresses much lower than the yield stress will cause negligible growth of all but the most severe defects under these conditions.

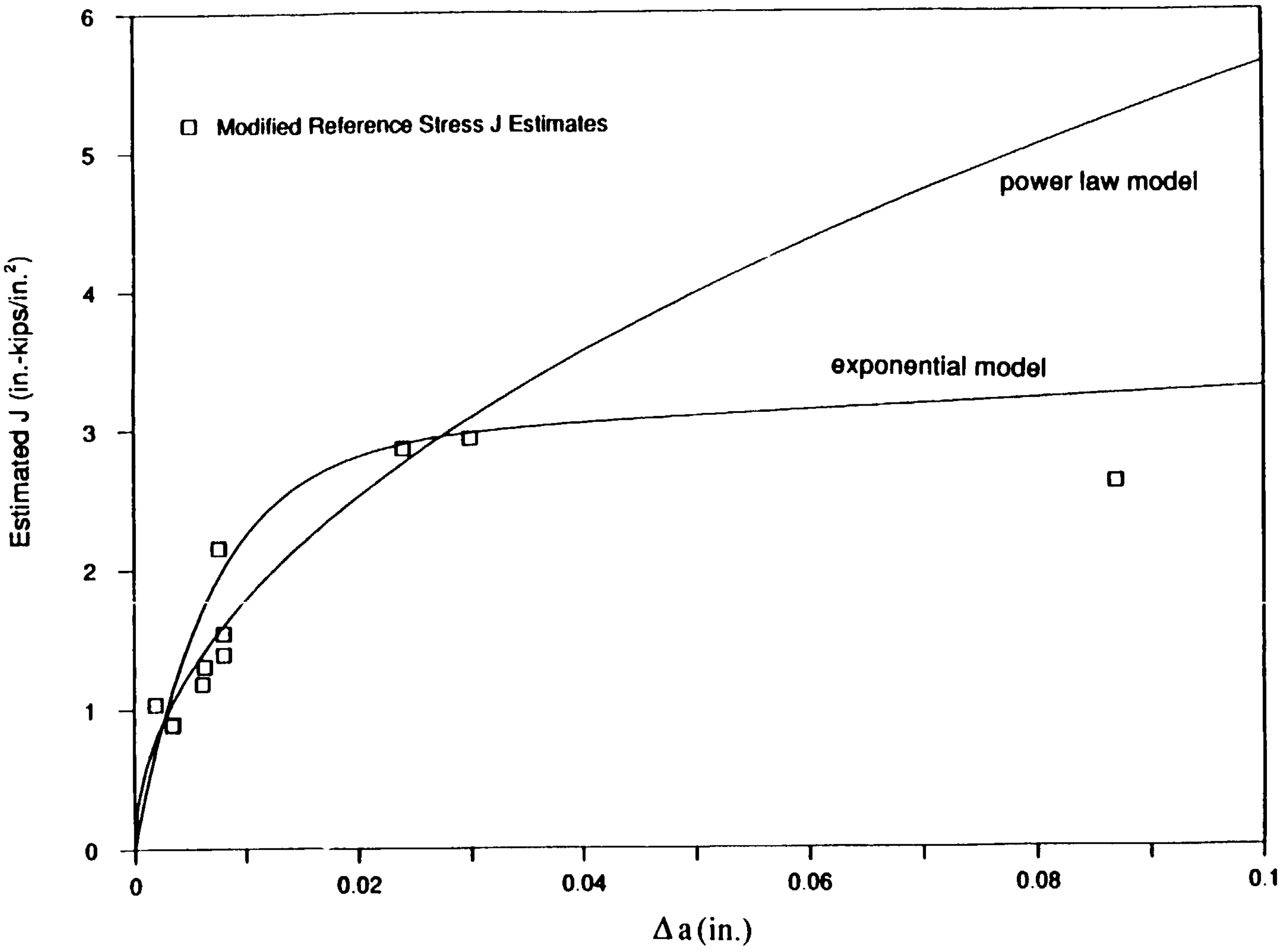

FIGURE 18. J Resistance curve for IN718 with semi-circular surface flaws: experimental data points based on modified reference stress J estimates and two different empirical models.

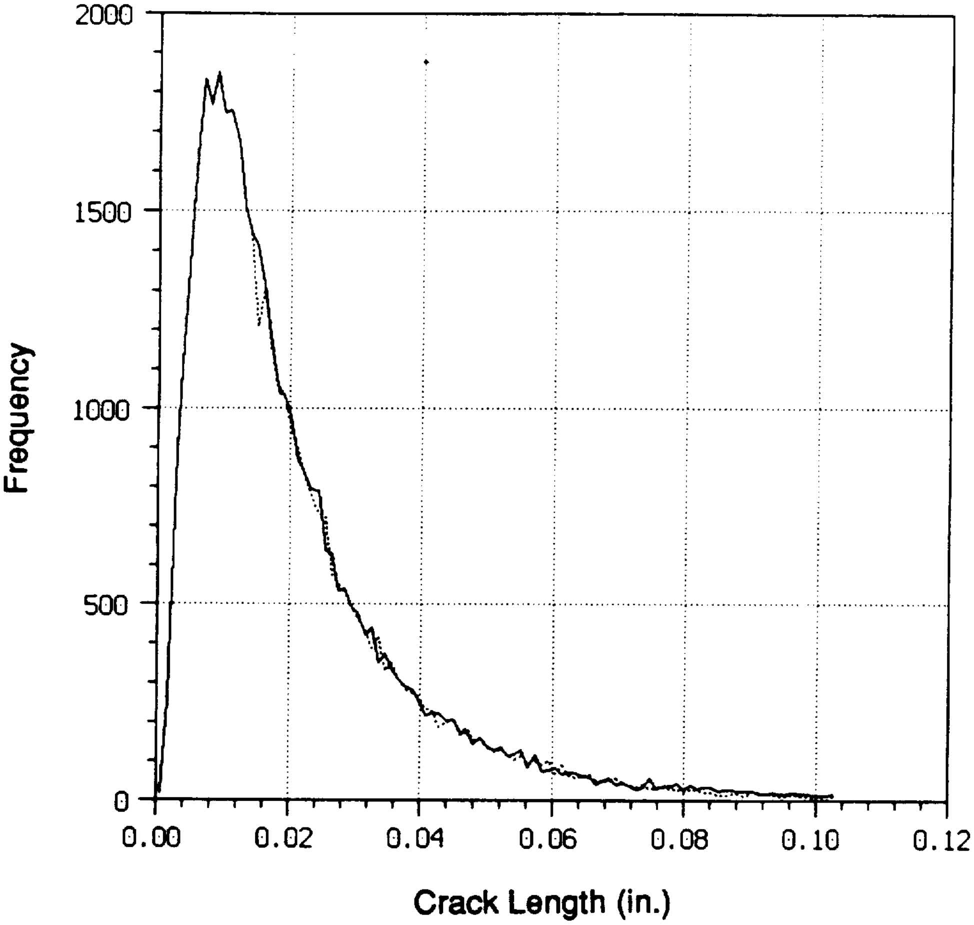

FIGURE 19. Initial (solid line) and final (dashed line) crack length distributions for simulated multi-cycle proof testing of surface-cracked IN718.

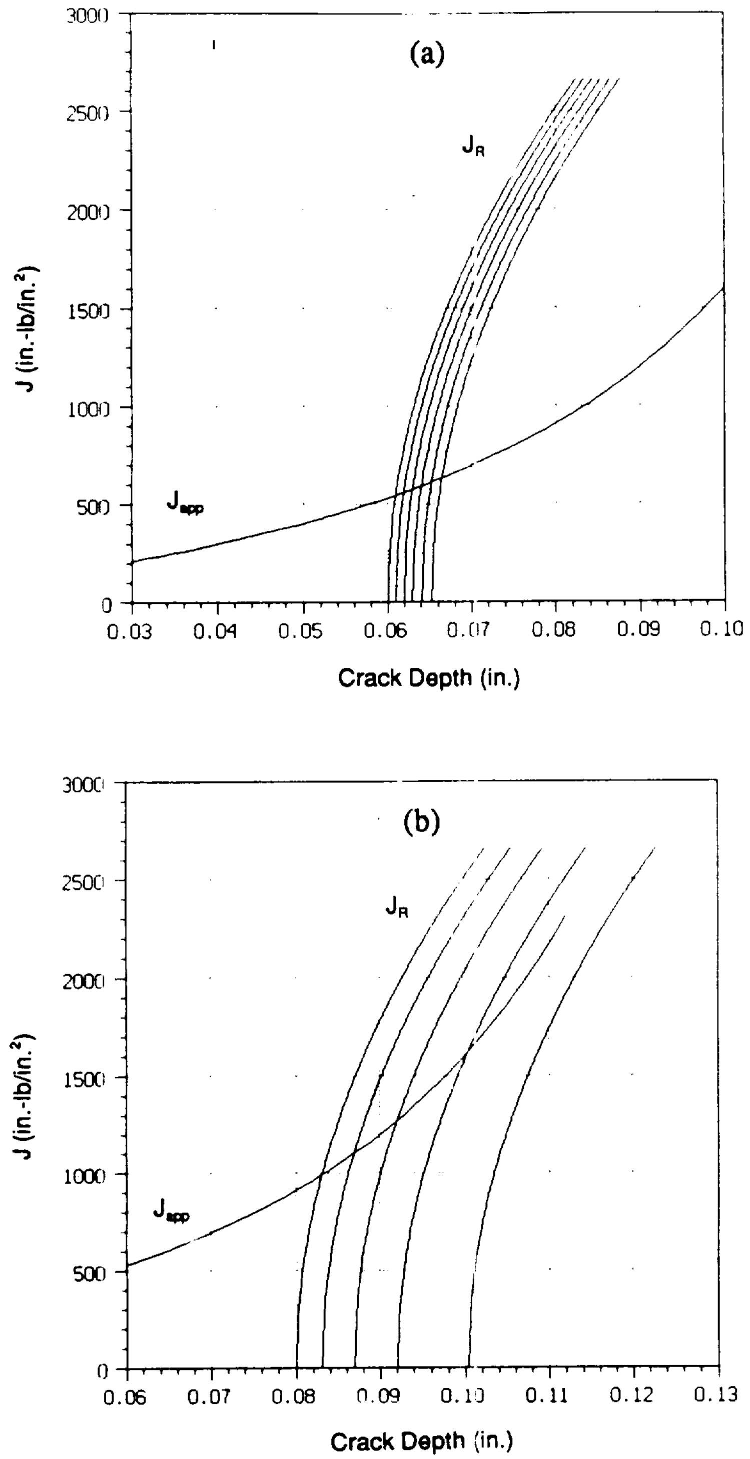

FIGURE 20. Simulated multi-cycle proof tests for surface-cracked IN718 with different initial crack depths.
(a) a_i = .06 in.
(b) a_i = .08 in.

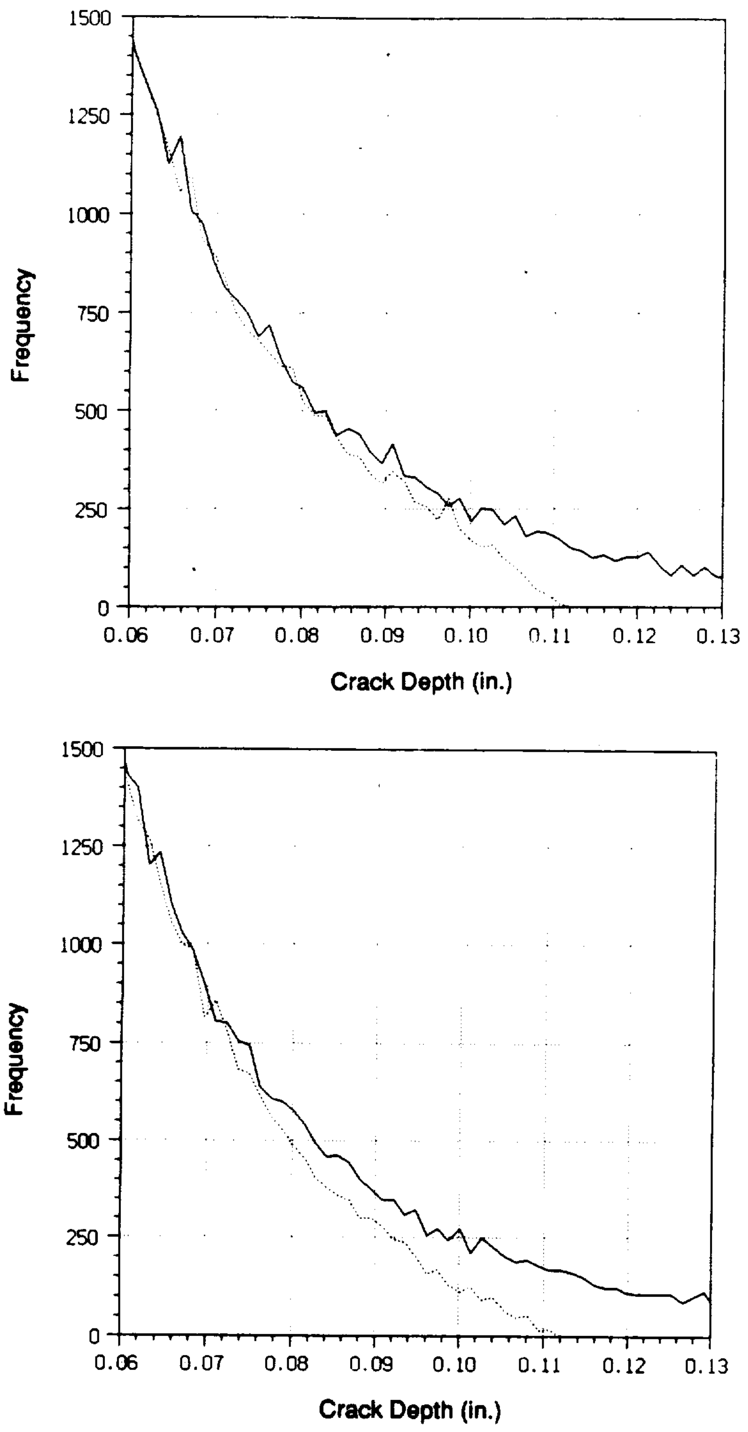

FIGURE 21. Right-hand tail of initial and final crack length distributions for simulated MCPT of surface-cracked IN718.
(top) one proof cycle
(bottom) five proof cycles

4. CRACK SIZE DISTRIBUTION FOR INCONEL 718 CASTINGS AND WELDMENTS

In order to model actual proof tests on SSME components, it is necessary to define relevant distributions of crack sizes and shapes. Data relative to initial defect sizes for SSME hardware or fabrication processes were collected at Rocketdyne. The data sources include material test coupons, selected SSME hardware, and available multi-cycle proof failure information.

From the initial defect size data, statistical distributions were defined to model the defect shape and size. Knowledge of these distributions will assist in choosing defect sizes for future laboratory proof testing experiments. Figure 22 is a frequency distribution of crack depth, a, and Figure 23 is a distribution of surface crack length $2c$. From these data, it can be seen that the largest concentration of crack depths are less than 0.02 in., while the crack lengths are less than 0.05 in. The frequency distribution of crack shapes, $a/2c$, is plotted in Figure 24. As expected, the predominant crack shape is semicircular ($a/2c = 0.5$). This crack shape is typical for predominantly tensile loading in this material, and the consistency of this shape as the crack grows will be verified during the experimental studies discussed next.

Figure 25 is a plot of the effect of crack depth on crack shape. While the first three plots fit well into either a Weibull or log-normal distribution, a correlation of the crack shape with size is less clearly defined, as seen in Figure 25. Almost all of the outliers in this figure ($a/2c > 2$) come from the electron beam welding (EBW) microfissure data. Not taking these data points into account yields a much more consistent crack shape to size correlation. While these flaw size distributions may provide the best simulation of actual flaw sizes in the SSME, decisions will still need to be made as to which flaw sizes will be used in the experimental proof testing to best verify the analytical results.

The Rocketdyne data on distributions of initial crack depth, a, were analyzed to determine the best statistical description. The Kolmogorov-Smirnov test was used to evaluate several different mathematical models, and the log-normal distribution with a mean value $\mu_x = 0.0212$ in. and a standard deviation $\sigma_x = 0.0203$ in. was determined to be the best description of the data (see Figure 22).

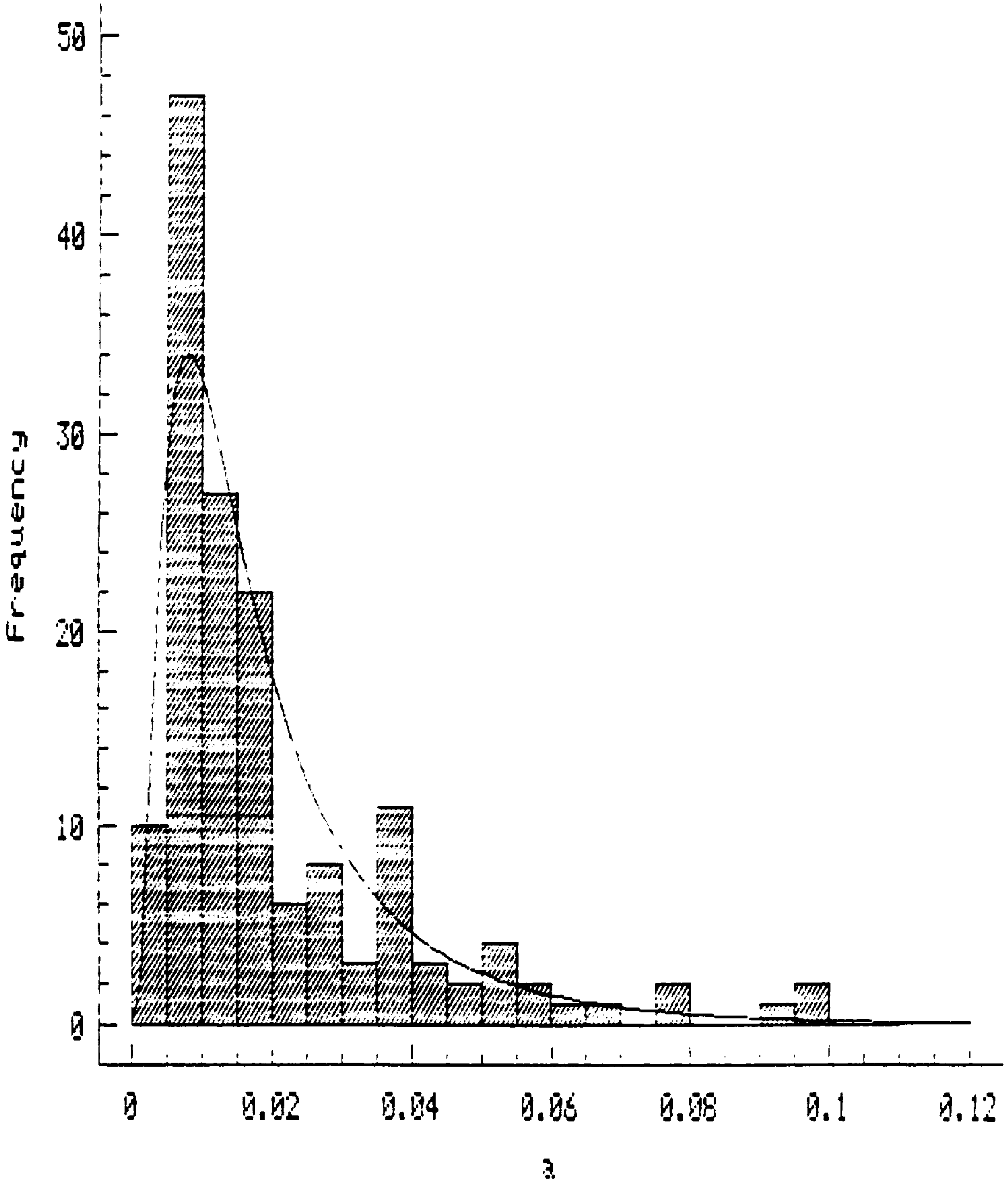

FIGURE 22. Distribution of initial crack depths.

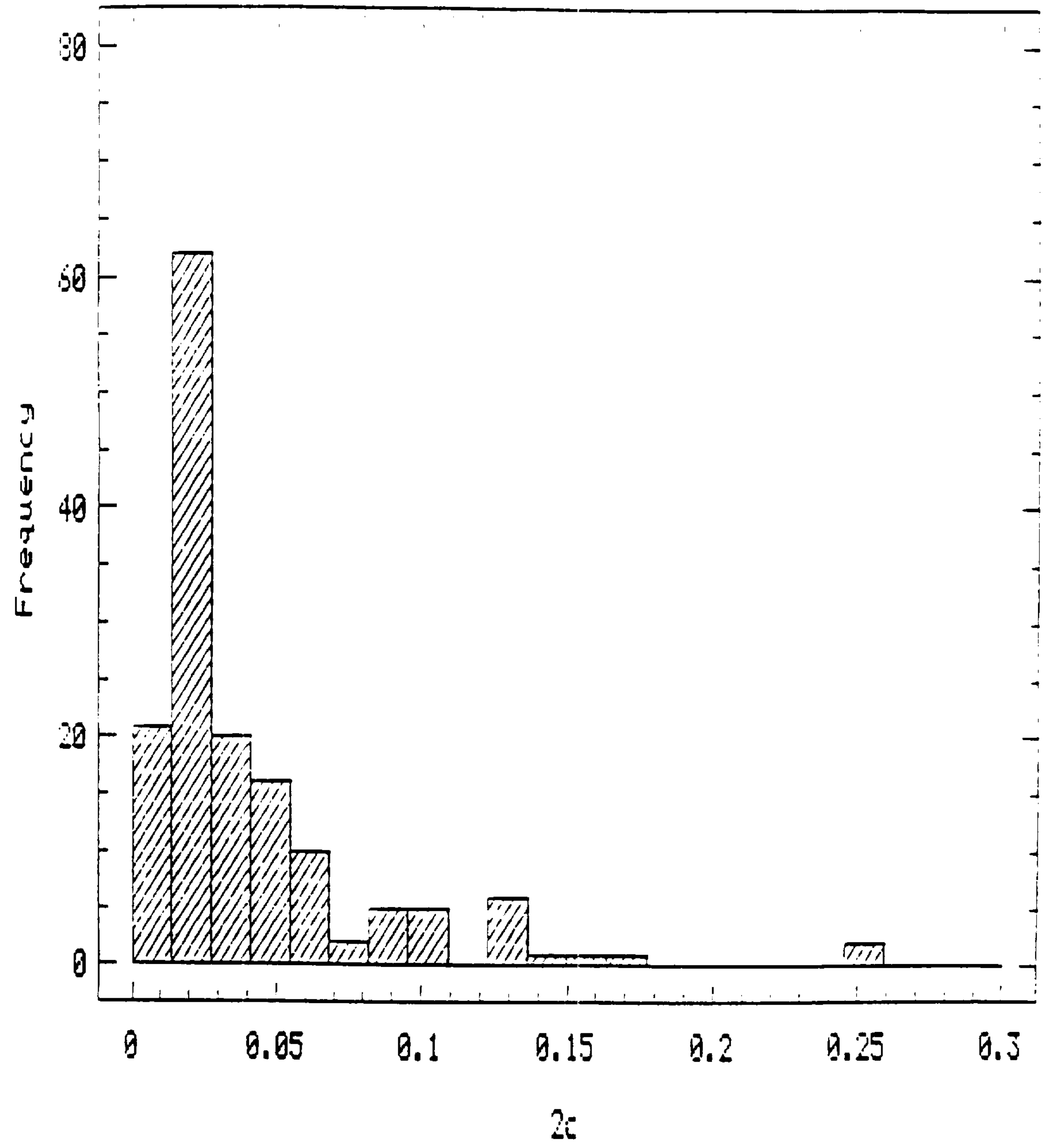

FIGURE 23. Distribution of initial crack surface lengths.

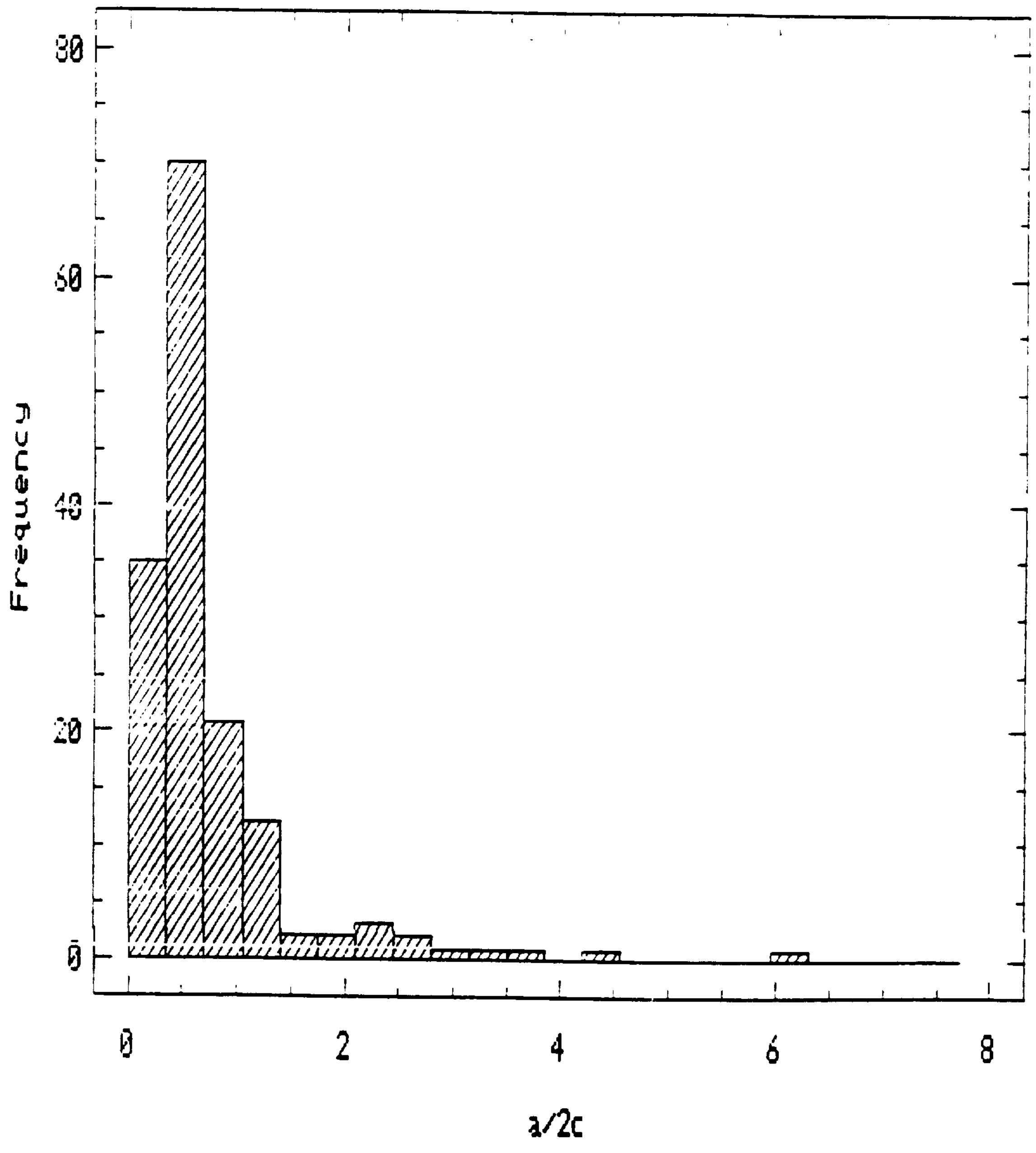

FIGURE 24. Distribution of crack shapes.

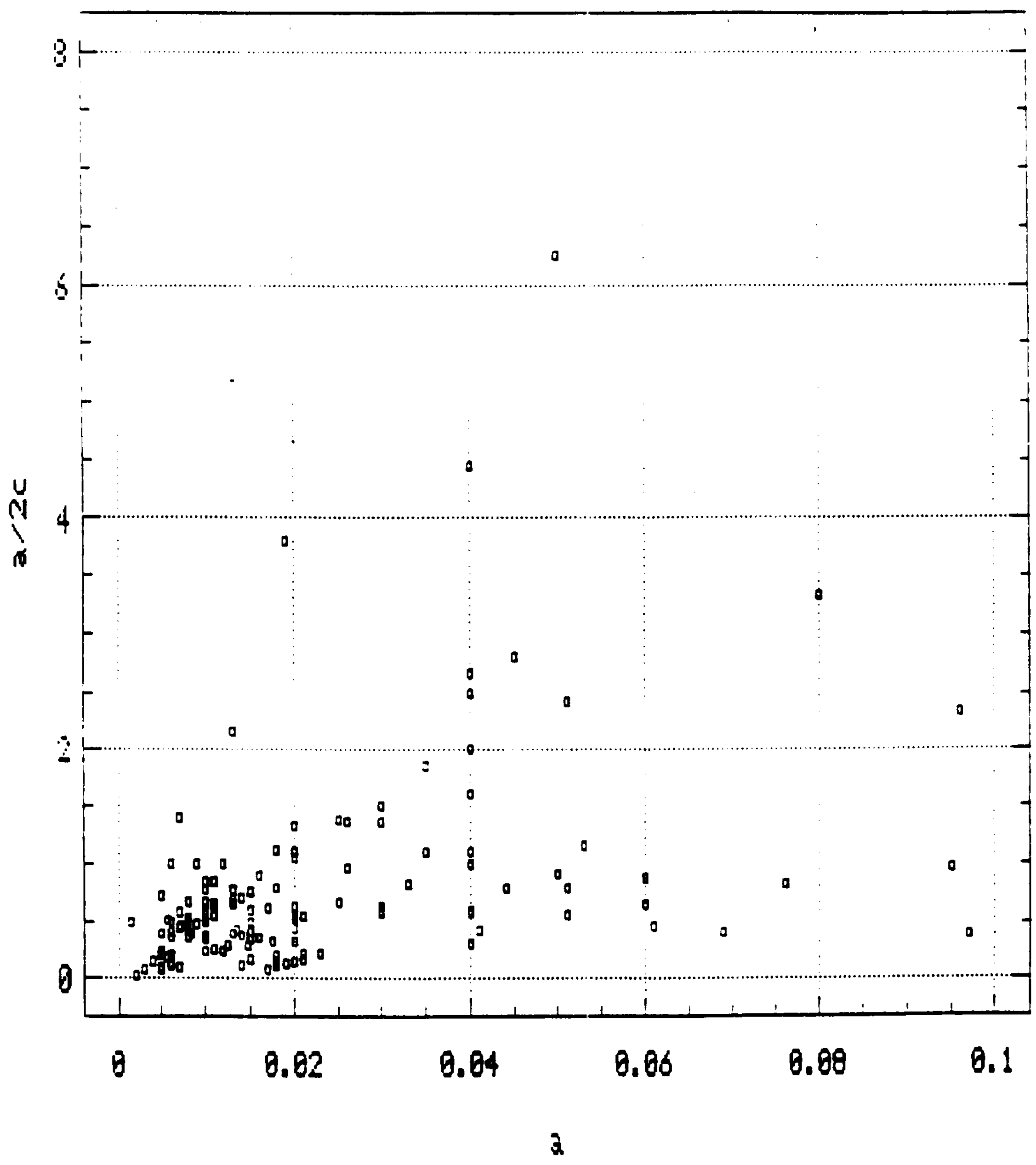

FIGURE 25. Effect of crack depth on crack shape.

5. FRACTURE MECHANICS PROPERTIES OF INCONEL 718

5.1 Material Characterization

Due to its wide application in SSME components, Inconel 718, a precipitation hardenable, nickel-base superalloy, was chosen for the experimental tests. Age hardening in this alloy is achieved through precipitation of a columbium-rich intermetallic phase which results in good corrosion and oxidation resistance, as well as good mechanical properties, which permit its use to temperatures of 1200°F.

Although most cracks in Inconel 718 components of interest to the SSME originate at welds, the current program examined base metal. This decision was made so as not to confuse the issue by the complexities associated with tests involving weldments--such as residual stress, out of plane cracking, and crack branching.

To ensure that the results generated were applicable to SSME components, the test material was purchased according to Rockwell Specification RB0170-153. The Inconel 718 was machined into "dog boned round" center cracked tension specimens, shown in Figure 26, and then heat treated by United Heat Treating Company according to the following procedures:

1) Rack parts to minimize warpage
2) Vacuum solution treat at 1900°F for 10-30 minutes
3) Argon back fill cool to room temperature
4) Age in vacuum at 1400°F for 10 hrs.
5) Furnace cool to 1200°F and hold for a total time (1400°F plus furnace cool plus hold time at 1200°F) of 20 hours
6) Argon back fill cool to room temperature

This particular heat treatment is used in SSME components to achieve optimum resistance to hydrogen embrittlement.

The chemical composition of the Inconel 718 material used is given in Table 3, and the basic mechanical properties are given in Table 4. These tensile tests results are in conformance with the RB0170-153 specifications.

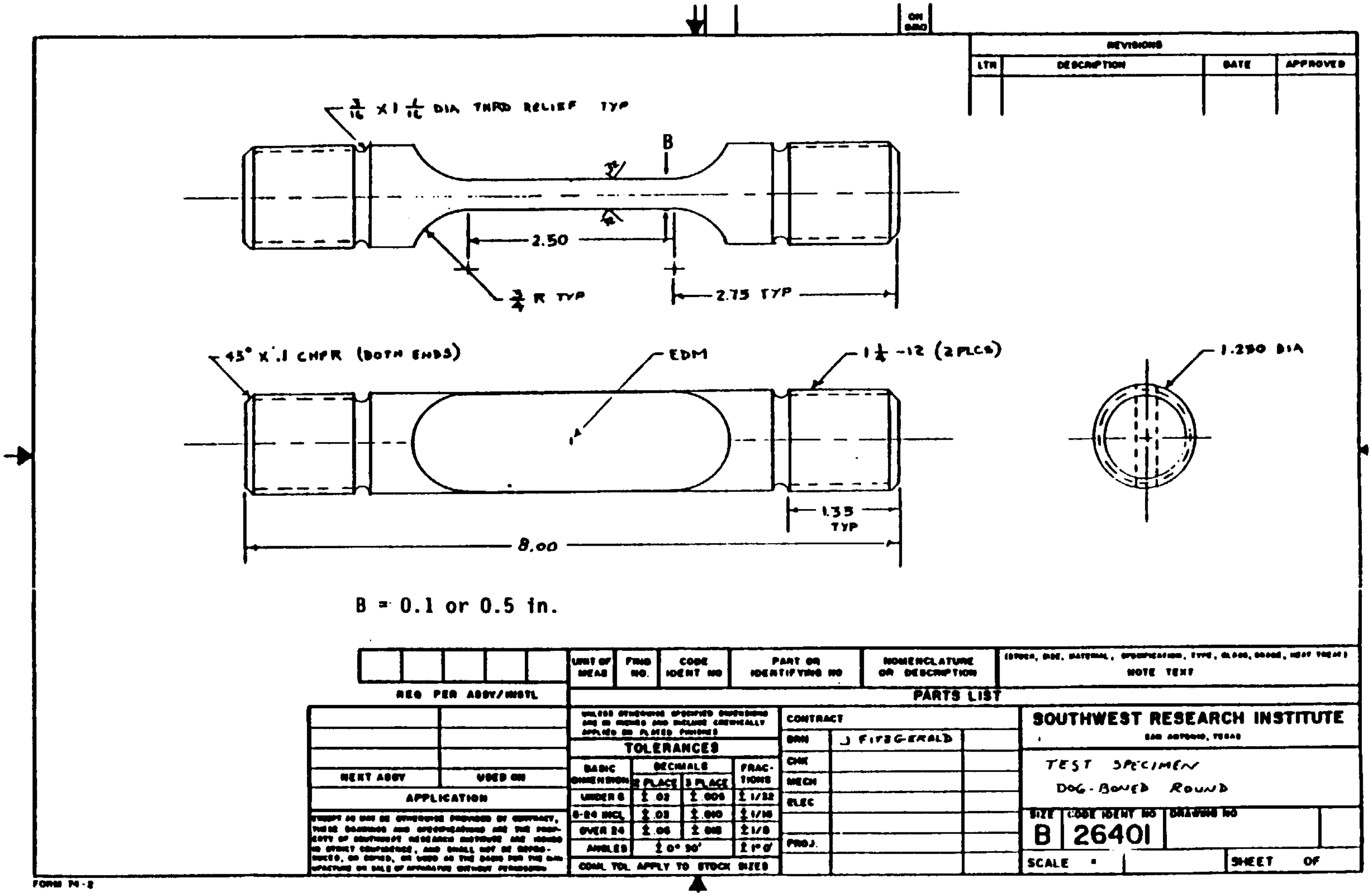

FIGURE 26. Surface-flawed specimen to be used in proof and fatigue testing.

TABLE 3

CHEMICAL COMPOSITION OF THE IN-718 TEST MATERIAL

Heat No.	C	Mn	Si	S	P	Cr	Ni	Mo	Co
6L9364	0.044	0.09	0.12	0.001	0.006	18.5	52.3	3.03	0.31
	Cu	**Al**	**Ti**	**Cb+Ta**	**Mg**	**Pb**	**Sn**	**Fe**	
	0.05	0.53	0.99	5.17	23 ppm	0.8 ppm	25 ppm	Bal	

TABLE 4

MECHANICAL PROPERTIES OF THE IN-718 TEST MATERIAL

0.2% Yield Strength, ksi	Ultimate Tensile Strength, ksi	% Elongation	% R.A.
161.2	205.5	22.2	33.3

5.2 Fatigue Crack Growth Rates

Fatigue crack growth rate tests were conducted on through-thickness cracked panels to determine both baseline fatigue data and information regarding fatigue range marking. This technique is based on the fact that the topography of the fatigue fracture surface is altered with changes in loading variables. The cyclic stress ratio $R^{\sigma} = K_{min}/K_{max}$ and ΔK can be changed to place a coarse mark on a fine surface, or vice versa, leaving a dark band on the fracture surface. The production of a well-defined range mark depends on prior knowledge of the fracture surface appearance. The crack growth rates correlated with the fracture surface morphology were used to select loading levels for the range marking necessary for the crack shape studies. Metallic materials exhibit a general fracture morphology trend of coarse-to-fine-to-coarse that occurs with transitions at crack growth rates of about 5×10^{-7} and 5×10^{-5} in./cycle, respectively.

Figure 27 provides a summary of the resulting crack growth rate data (da/dN) plotted as a function of the crack-tip stress intensity factor range (ΔK) for three specimens. Two tests were run on 0.2 in. thick specimens to provide data over a wide range of growth rates. As indicated by the figure, the data obey a power law above $\Delta K = 10$ ksi$\sqrt{\text{in.}}$, with good agreement in the mid-range where results from the two specimens overlap. The third test was conducted on a 0.5 in. thick specimen. Results from the two thicknesses are in excellent agreement, except in the region near $\Delta K = 65$ ksi$\sqrt{\text{in.}}$ The deviation in this region is believed to be due to the occurrence of noticeable crack branching in the 0.2 in. thick specimen, which apparently resulted in retardation of the growth rates in this specimen.

Visual examination of the fracture surfaces of the above experiments revealed significant differences in the fracture surface morphology at high and low growth rates. This observation provides verification that range marking can be successfully employed to mark crack extension in the following experiments on surface-cracked specimens.

5.3 Surface Crack Shape

Crack-shape studies were conducted to determine the shape of the crack as it grows. Fatigue range marking bands were used to both verify changes in the crack shape and monitor the crack growth during the R-curve determination.

All specimens are first polished down to a 1 micron diamond polish to provide easy viewing of the crack during the test. Electro-discharge machining (EDM) slots were introduced into the surface of the specimens to provide a starter for the crack. The slot sizes for the 0.2 in. thick specimens were 0.05 in. deep by 0.100 in. long and in the 0.5 in. thick specimens they were 0.125 in. deep by 0.25 in. long. Prior to the precracking, the specimens were prepared with photographic grids, having 0.010 in. spacing, to provide reference lines for the visual crack length measurements. Three specimens were then precracked and tested under fatigue loading at a stress ratio of 0.1 using a closed-loop, servo-hydraulic testing machine.

Crack shape study experiments were conducted on surface flawed 0.2 in. thick specimens. Crack opening displacement (COD) was measured with a clip gage, having 0.2 in. gage length, positioned on diamond indentions located just above and below the EDM flaw. The shape of the growing crack was periodically marked using fatigue range marking. On the first attempt at range marking, fine marks were applied to the fracture surface. When

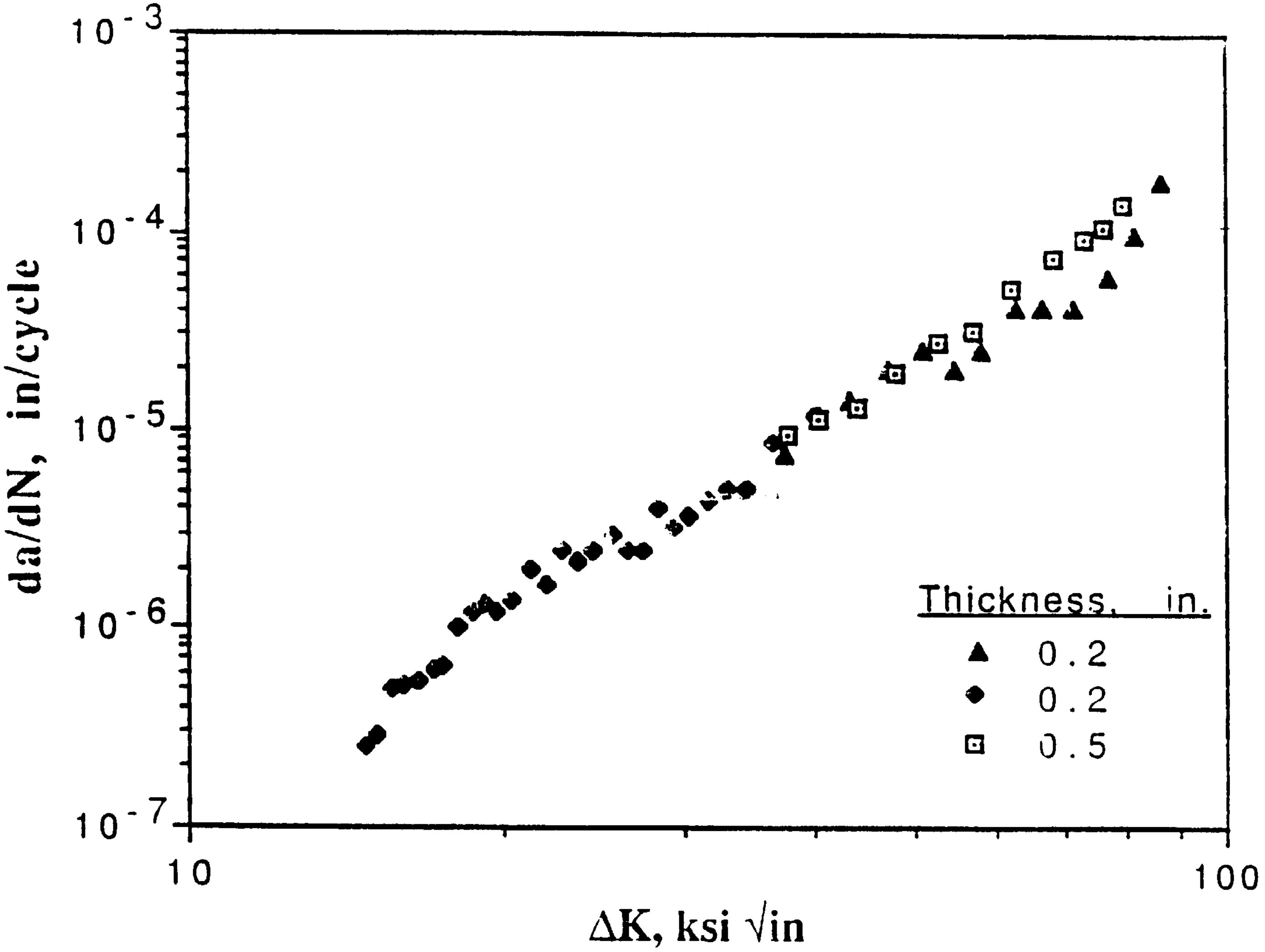

FIGURE 27. Crack growth rate data for Inconel 718.

the specimen was broken open, these marks were indistinct, indicating that a coarser marking was necessary. For the second attempt, a coarse-on-fine scheme was employed to produce the marker band. The stress ratio chosen to produce a marker band (R_x^σ) was estimated from the following empirical relationship:

$$\frac{(da/dN)_{Ref(R^\sigma=.1)}}{(da/dN)_{mark}} = \left\{ \frac{1 - R_{Ref}^\sigma}{1 -- R_x^\sigma} \right\}^2 \tag{18}$$

where d*a*/d*N*(mark) was chosen to be 1 x 10^{-7} in/cycle and R_x^σ was determined for each reference d*a*/d*N*. Prior to marking the specimen, the load was dropped 30%. This drop in maximum load is desirable during the proof tests, so that only small crack extension will occur during the marking.

First, a through-crack specimen was fatigue range marked, as shown in Figure 28, then a part-through flawed specimen, as shown in Figure 29. To allow for more accurate measurements of the fracture surface, the photograph of the part-through crack fracture surface was enlarged and the range marking bands were darkened, as shown in Figure 30. One of the more noteworthy pieces of information attainable from this figure is the nearly constant crack shape of 0.5. The shape varies from 0.493 to 0.549 at the seven marker bands, as shown in Figure 31, holding the nearly semicircular shape throughout the growth of the crack.

5.4 Surface Crack J-R Curve

Resistance curves were generated for surface-cracked panels of Inconel 718 under both load and displacement control. Because of the high toughness of this material (approximately 130 ksi$\sqrt{\text{in.}}$), all specimens exhibited net section yielding before the onset of instability. This situation has required the use of elastic-plastic analysis techniques to establish the resistance curve, as discussed in the analysis section below.

5.4.1 Experimental Procedures

The load control experiments are defined as those where the applied load was used as the feedback signal for the servo-hydraulic test machine. During these tests, a COD gage was connected to either side of the EDM flaw, with a gage length of 0.200 in. Two methods were attempted to monitor crack extension during loading: 1) changes in elastic compliance during periodic unloading of the specimen; and 2) fatigue marker bands introduced by periodic cyclic loading at a high R ratio. However, due to the small amount of crack extension which occurred in the experiments, crack extension could not be reliably detected with these techniques. Nevertheless, it was possible to generate a resistance curve by testing multiple specimens. In each case, the specimen was loaded to produce different amounts of crack extension as determined by post mortem analysis of the fracture surface. Only small amounts of crack extension (< 0.008 in.) were obtained in any of these load-controlled tests. Thus, the load-control tests do not adequately simulate the substantial crack extension which can occur during the proof testing of actual SSME components. That is, instability intervenes before much crack growth can be achieved.

ORIGINAL PAGE
BLACK AND WHITE PHOTOGRAPH

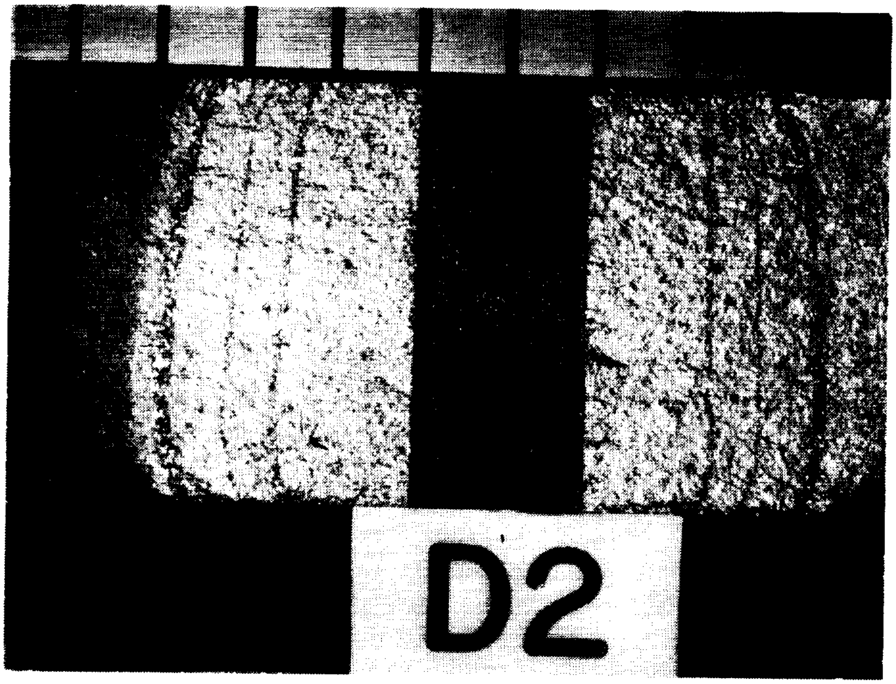

FIGURE 28. Fracture surface of a range marked through-crack specimen.

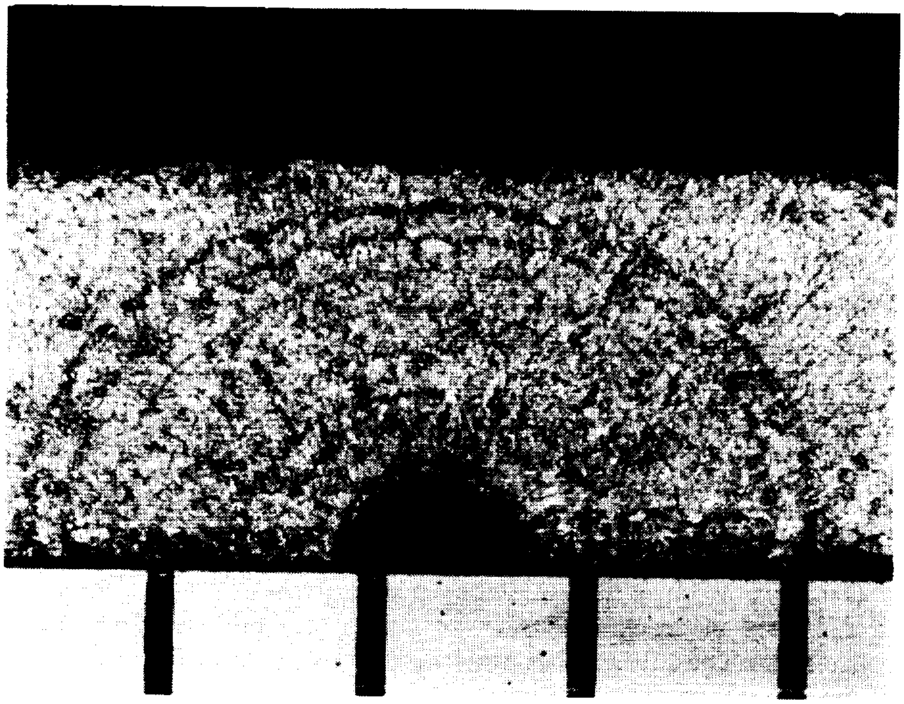

FIGURE 29. Fracture surface of a range marked part-through crack specimen.

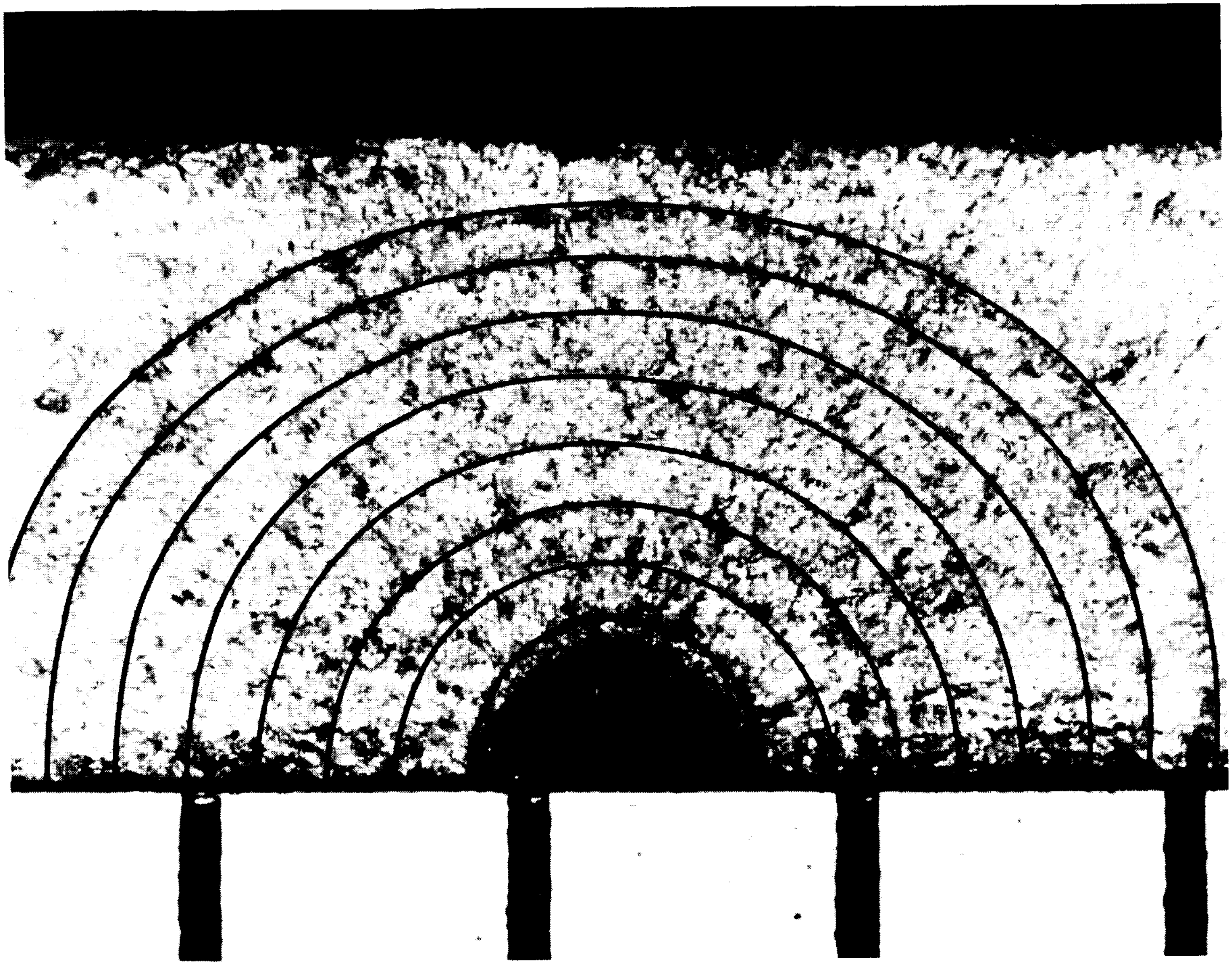

FIGURE 30. Enlarged fracture surface of part-through crack specimen.

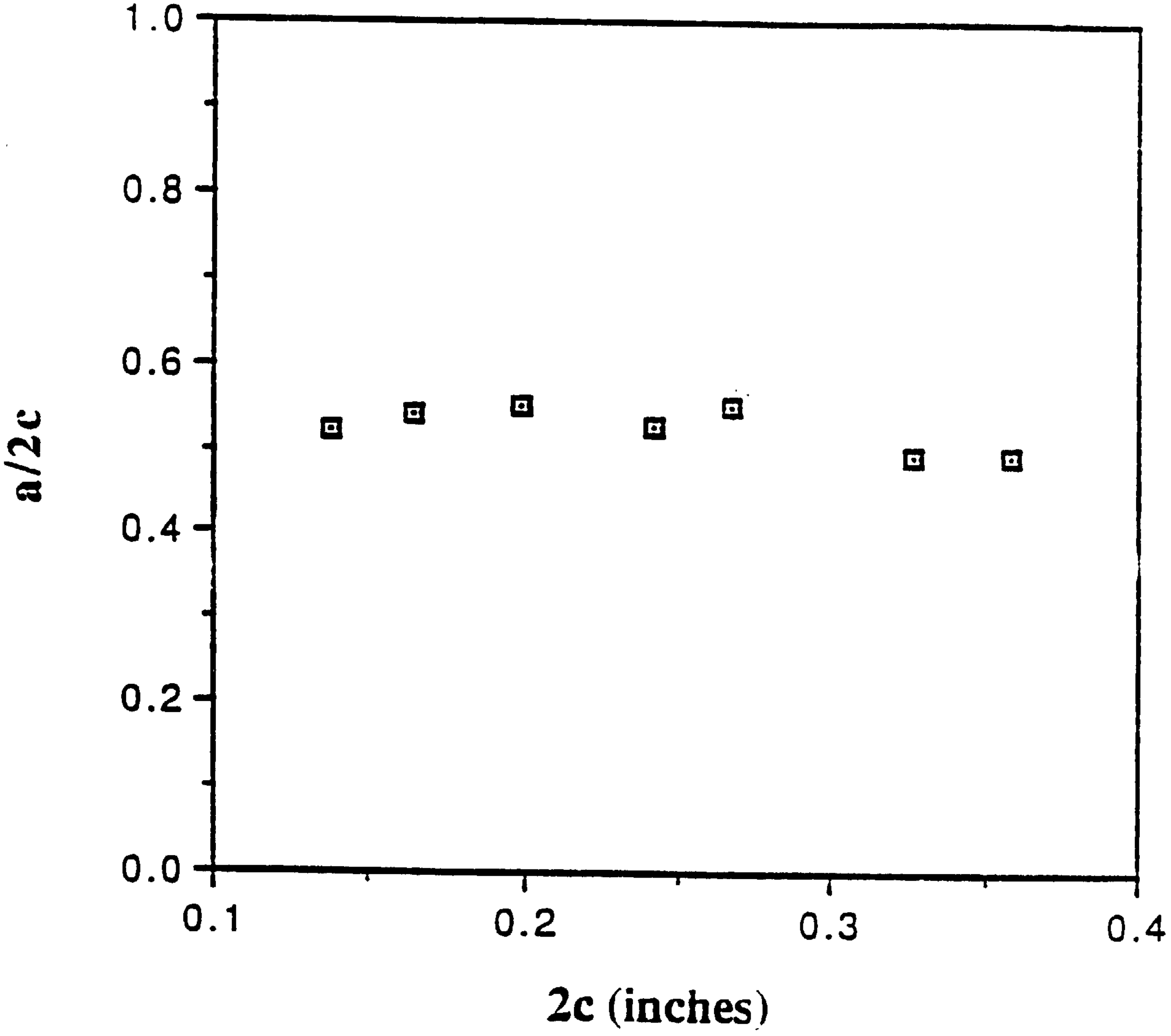

FIGURE 31. Variation of crack shape with crack size for Inconel 718.

The other limiting type of test for the *R*-curve experiments is a displacement-controlled test. During these tests, the specimen was driven to a set displacement, allowing the load to increase as necessary to reach that displacement. In this case, the COD gage was modified to obtain a gage length of 0.05 in. By conducting the test in this manner, one can achieve virtually any displacement (and thus crack growth), since the applied *J* decreases as the crack extends. For the displacement-controlled tests, larger Δa values were thus obtained than in the load-controlled tests. The actual SSME components will instead see a loading somewhere between the two limiting cases of load and displacement control.

5.4.2 Procedure Used to Analyze *J-R* Curve Data

Material Properties for Inconel 718. Application of the reference stress approach for *J* estimation requires development of a closed-form estimate for the constitutive relationship. Analysis of load-displacement records from SwRI tensile tests of Inconel 718 yielded a relationship between stress and plastic strain of the form

$$\sigma = 248.4\varepsilon_p^{0.0633} \tag{19}$$

The elastic modulus is 29.69 x 10^3 ksi. The relationship between stress and total strain may also be written in the general Ramberg-Osgood form, Eqn. 13, where $\varepsilon_0 = 0.006$, $\sigma_0 = 179.8$ ksi, $\alpha = 1$, and $n = 15.8$.

Resistance Curve for Inconel 718. Resistance curve data for Inconel 718 obtained by Rocketdyne from relatively thick ($B = 0.6$ in.) compact tension (CT) specimens were supplied to SwRI. Non-linear least squares regression techniques were used to obtain best fits to the different empirical *J-R* curve models mentioned above. These empirical models included four equations proposed by Orange [29], as well as a power law. The data and some of the different fits are shown in Figure 32. None of the four models were clearly inferior or superior in their ability to describe the data. While correlation coefficients varied somewhat, all were around 0.900 - 0.940. The choice of a specific model is a matter of mathematical convenience and personal judgement about which model captures the most important features of the data. Note that the average value of the tearing slope was 3400 in.-lb/in., which yields a value for the tearing modulus of only about 3.1 -- indicative of a material with relatively low ductile tearing resistance.

The resistance curve for Inconel 718 in the surface-cracked configuration is not necessarily the same as the CT resistance curve due to variations in stress state, as manifested by both global geometry and crack geometry. It is possible to construct a *J-R* curve for surface cracks in IN 718 from the limited number of tests conducted by SwRI and discussed in Section 5.4.1. The primary difficulty lies in calculating the appropriate *J* value for a given load-displacement record and increment of crack growth. Traditional schemes for calculating *J* from load-deflection records of CT tests are well-established, but corresponding schemes for complex geometries such as the surface flaw have not yet been proven.

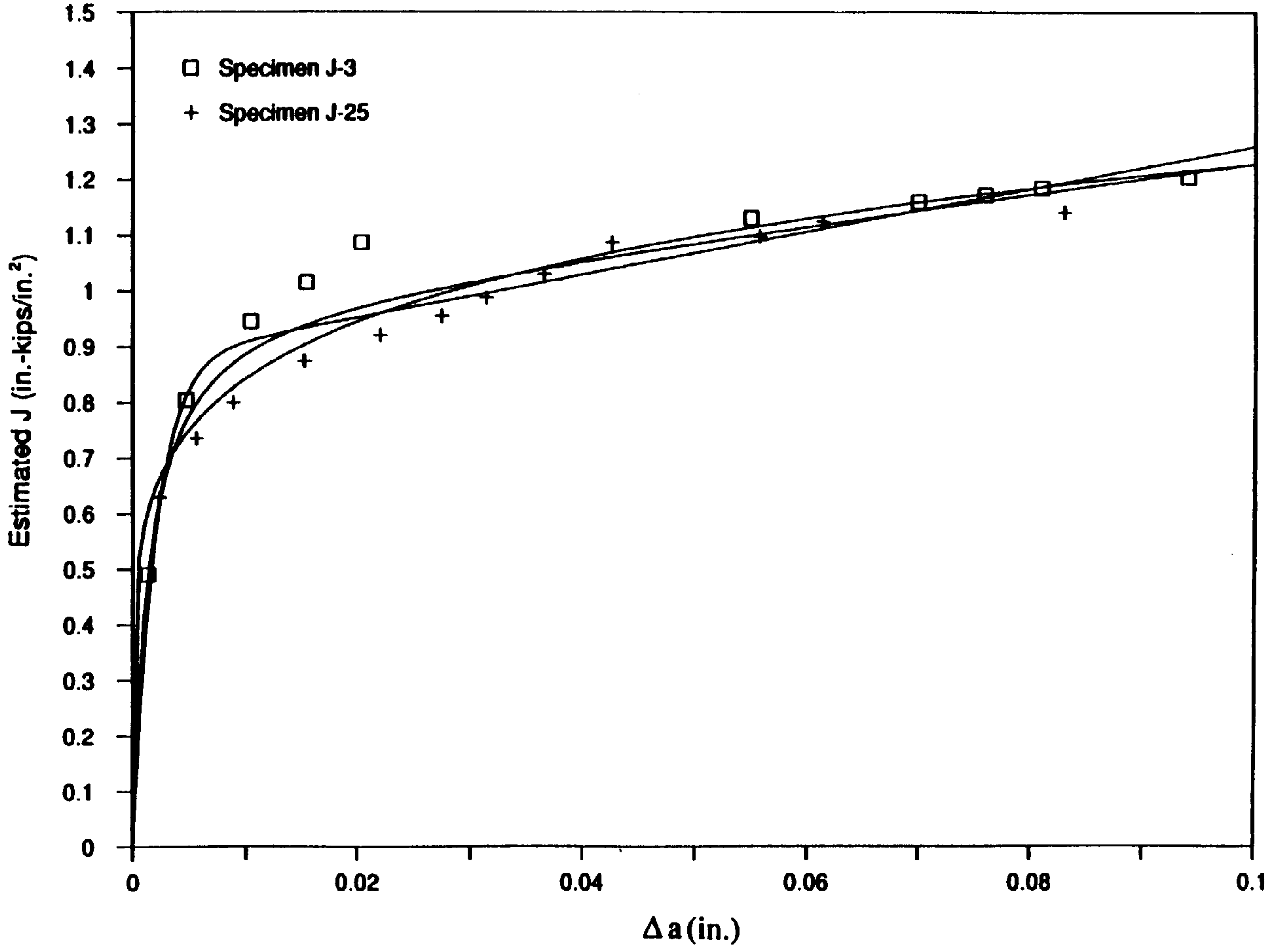

FIGURE 32. Elastic-plastic J-R curve for Inconel-718 based on Rocketdyne CT data. Lines shown are best fits to three different empirical models.

Two approaches are available to estimate J for these tests. The first uses the modified reference stress technique described above in Section 3.3. This scheme depends only on the final load and crack length and not on the load-displacement history. The second scheme is an "equivalent energy" approach utilized recently by McCabe [38]. He suggested that J could be calculated as:

$$J = \frac{(K_R)^2}{E} \tag{20}$$

where K_R is a plasticity-modified stress intensity factor given by

$$K_R = K_{Ie}\sqrt{\frac{A_T}{A_e}} \tag{21}$$

Here A_T and A_e are the total and elastic areas under the load-displacement curves and K_{Ie} is the linear-elastically determined stress intensity factor; see Figure 33.

The resulting estimated resistance curve estimates for the surface cracked Inconel 718 are shown in Figure 34, along with the CT resistance curve. Note that the modified reference stress and equivalent energy estimates gave similar values for J, typically differing by about 10%. The primary exception to this agreement is the data point corresponding to the displacement-controlled test with the greatest amount of crack extension. This may reflect the uncertainty associated with J following large amounts of crack advance with associated elastic unloading in the wake of the crack.

The resistance curve for surface cracks is clearly different from the resistance curve for CT geometries. The initial slope (associated with the blunting line and early crack growth) appears to be about the same, but the critical J value at which large amounts of crack extension begin to occur is much higher. This indication of higher toughness is consistent with a possible change from high constraint in the thick section CT tests to lower constraint in the thin section, deeply cracked surface flaw tests. Other factors may also be involved, including the loss of J-dominance (discussed further below). Similar behavior was previously observed by White, Ritchie, and Parks [39]. Furthermore, there appears to be a more gradual change in the slope of the surface crack resistance curve in the vicinity of the "knee". It is difficult to evaluate the possible changes in the tearing slope with specimen geometry in this case, since only a few points are available to calculate this slope for the surface crack tests. It is possible that the tearing modulus remains unchanged with the specimen geometry, but it is also possible that the tearing modulus increases (perhaps due also to loss of constraint) for the surface crack. Both phenomena have been reported in the literature for other materials. Further tests may be needed to better characterize the tearing slope, particularly for small amounts of crack extension.

In one sense, the uncertainties associated with J estimation for development of the resistance curve are not fatal. Since analysis of crack growth involves comparison of applied J and material resistance J, the important issue is to be consistent in the way the two values are estimated. Absolute errors in the estimation scheme will, to some degree, cancel each other out.

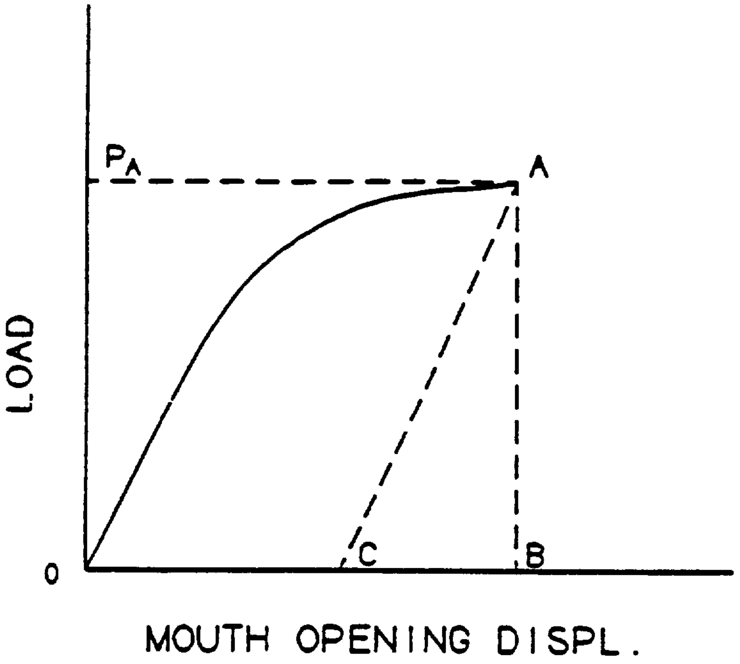

$$K_R = (K_{Ie})_A \sqrt{\frac{A_T}{A_e}}$$

Where $(K_{Ie})_A$ is linear-elastic K determined using load P_A

A_T = Total Area (O-A-B)

A_e = Elastic Area (C-A-B)

FIGURE 33. Illustration of equivalent energy method for estimating J for surface cracks (taken from [38]).

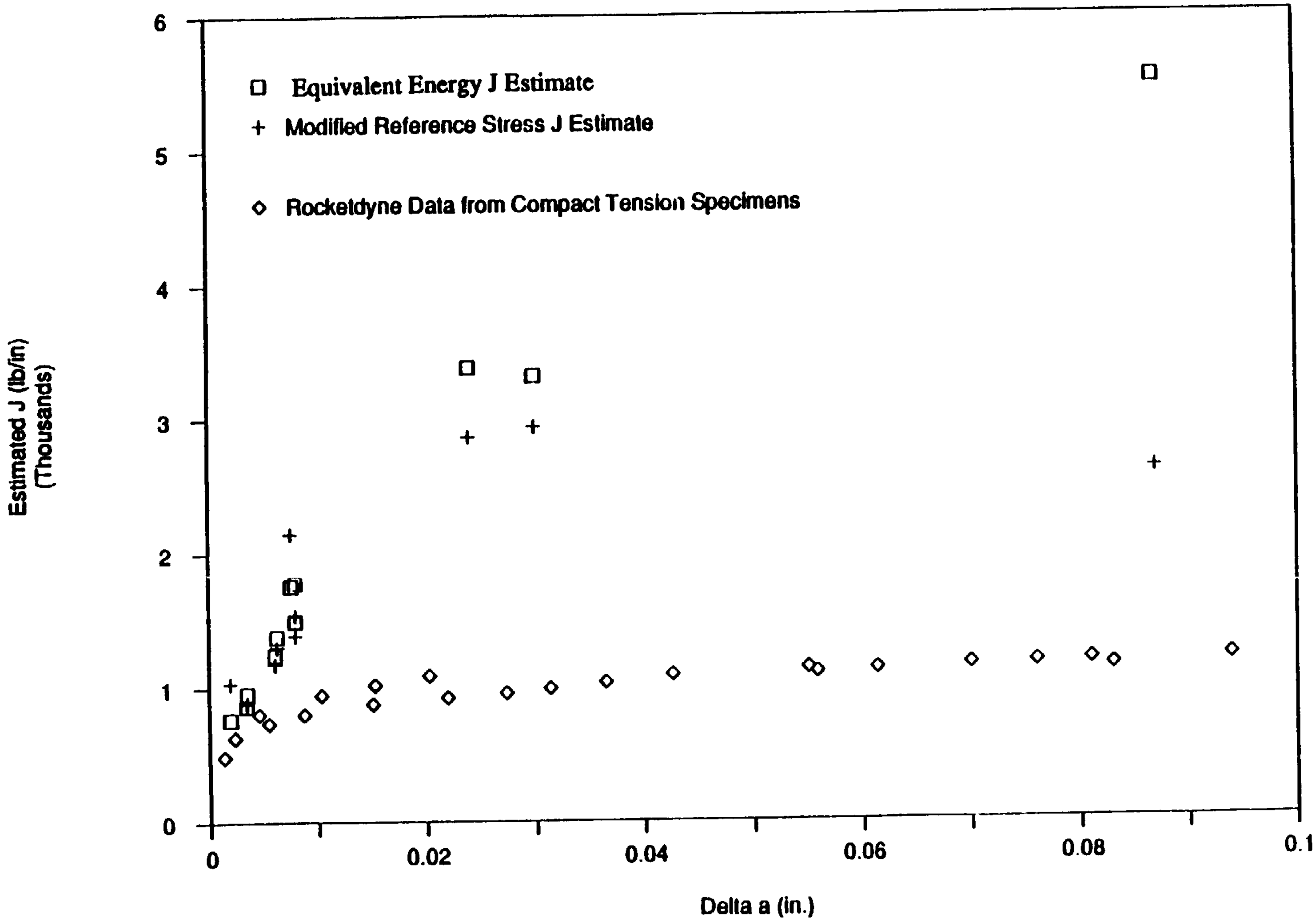

FIGURE 34. Resistance curve data for IN-718 surface cracks based on two different J-estimation methods and compared with CT data.

6. DISCUSSION

It appears that the selection of an optimum proof test strategy, including specification of the optimum number of proof cycles, will depend on several crucial factors. The nature of local control (load vs. displacement) in the actual component will be of great importance. While traditional pressure testing is consistent with load control, the development of local plasticity in net sections is likely to lead to some local intermediate control condition analogous to Neuber control at the root of a notch. Identification of this control condition and appropriate mathematical description are essential to development of the proper proof test strategy. This will require elastic-plastic stress analysis of the cracked component itself. Consideration must also be given to the nature of the material resistance curve, including the initial slope, the effective J_{Ic} value, and the tearing modulus; the initial crack size distribution; and the magnitude of the applied loads/displacements. Therefore, selection of an optimum proof test strategy may be specific to each component (considering geometry, material, and design loads).

Several other important questions remain unanswered, however, and should be addressed in further experimental and analytical research. What really happens during unload/reload cycles? When does further ductile tearing or accelerated fatigue crack growth occur or not occur? What is the relationship between fatigue and tearing? Does the resistance curve actually regenerate itself consistently on subsequent proof cycles by moving along the Δa axis? Or are there other changes in the shape or origin of the resistance curve? How does the resistance curve change with specimen and crack geometry? A major change was observed between the thick CT geometry and the thin plate surface crack geometry. Will further changes occur from component to component? Do resistance J values change around the perimeter of a surface crack? Applied J values are known to change around the perimeter. Must this be considered more rigorously? Are J_{app} and $J_{resistance}$ consistent on each cycle? Or does material hardening during the first cycle cause changes in these values for subsequent cycles? How does J change for extremely deep surface flaws, or for flaws which have experienced large tearing?

Another set of questions and unresolved issues relates more directly to the validity of J as the governing fracture parameter for large cracks and high applied stresses. The J-integral accurately expresses the magnitude of the near-tip stresses and strains when the Hutchinson-Rice-Rosengren (HRR) singular fields dominate the complete crack-tip fields over distances large compared to crack-tip blunting and fracture process zones. But as stresses and strains increase towards a fully plastic load state, constraint is lost and the HRR fields no longer dominate. Parks and Wang [33] have recently studied this problem in some depth for the three-dimensional surface crack. They found for two specific crack geometries that HRR-dominance slowly deteriorated until applied stresses approached the flow stress, when loss of dominance accelerated rapidly. Even the semi-circular flaw, which is ordinarily associated with a high level of constraint, exhibited in-plane plastic flow deformation patterns in the remaining ligament typical of single edge cracks under tension. No rigorous criteria have yet been forwarded, however, to characterize loss of dominance for three-dimensional configurations with respect to specific geometries or load levels. Furthermore, it is not yet entirely clear what loss of dominance might mean in a pragmatic sense to assessment of tendencies for ductile fracture of surface cracks. Although J may lose its rigorous meaning as the characteristic parameter for the near-tip stress-strain field, might it still be useful in an engineering sense to describe crack growth?

Some of these questions introduce pragmatic issues related to the engineering application of the analysis method. The analytical model requires acceptably accurate *J* estimates for cracks in actual hardware, and these geometrical crack/component configurations are typically more complicated than the handbook-type solutions commonly available. The reference stress method used in this study appears to hold considerable promise for the efficient solution of more sophisticated problems, but further study is needed. A second major input required by the analytical model is resistance curve data for crack geometries of interest in materials of interest. In view of the geometry-dependence of the *J-R* curve exhibited here, a library of CT resistance curves may be of limited value. There are obvious practical limits on the number of original resistance curves which can be generated for different geometries, however. Some advances in the theoretical understanding of geometry effects on the resistance curve are needed.

Still other, perhaps more fundamental, questions remain to influence the practice of MCPT in an actual production/service environment. How does crack growth during proof testing influence subsequent fatigue crack growth during normal service? Will MCPT lead to retardation - or acceleration - of crack growth when the component sees typical service histories? How do resistance and applied *J* values change for irregularly shaped flaws in inhomogeneous weldments? And are there other factors which may contribute to failure during MCPT, such as the transformation of some material defect into a true crack after several cycles?

7. CONCLUSIONS AND RECOMMENDATIONS

1. Based on a survey of MCPT experiences, as well as experiments on surface-cracked Inconel 718 panels, it is concluded that stable crack growth during MCPT involves significant plastic deformation. In components, this deformation occurs locally in uncracked ligaments associated with cracks which are large compared to the component thickness.

2. Based on a statistical analysis of data compiled from SSME components, as well as welded and cast Inconel 718 specimens, it is concluded that incipient crack depths are log-normally distributed with a mean of 0.021 in. and a standard deviation of 0.020 in.

3. Based on a newly developed analytical model of MCPT, combined with Monte Carlo simulation techniques, it is concluded that the changes in the crack size distribution during MCPT depend on the interaction between the number of proof cycles applied, the nature of the J-R curve (both J_{Ic} and tearing modulus), the initial crack size distribution, the component boundary conditions (that is, load control versus displacement control), and the magnitude of the applied load or displacement.

4. In view of the above factors, the relative advantages and disadvantages of single-cycle versus multi-cycle proof testing will, in theory, be specific to component geometry, material, and fabrication technique.

5. Components whose boundary conditions, local to the cracked region, approach load control during proof testing are more likely to be amenable to successful MCPT, whereas those approaching displacement control should not be subjected to MCPT, particularly where leaks cannot be tolerated.

6. Ultimately, the assessment of the relative merits of MCPT will require elastic-plastic analysis of representative components containing representative large cracks, since the actual loading is somewhere between load and displacement control.

7. Further progress in understanding and optimizing MCPT depends on clarification of the following fundamental issues:

   a) the dependence/independence of the J-R curve on specimen (or component) geometry, including crack size and shape;

   b) the variance/invariance of the J-R curve for large unloading cycles;

   c) The possibility of variations in applied J for surface flaws which are extremely deep or which have experienced substantial ductile tearing;

   d) The interaction of applied and resistance J for multi-degree-of-freedom crack configurations in which both J_{app} and J_R may change around the perimeter of the crack.

8. The engineering application of the analytical model developed herein for MCPT depends on:
    a) the availability of *J* estimates for surface-cracked components; and
    b) the availability of *J-R* curve data for surface cracks in materials of interest.
9. The next step in developing a MCPT strategy should involve a coordinated experimental-analytical effort focusing on the experimental validation of the assumptions of the present analytical model, with deviations between measured and predicted behavior serving as the basis for model improvements.

REFERENCES

1. J. Mendoza and G. A. Vroman, "Multiple Cycle Proof Test Logic," Rocketdyne Internal Report SSME 73-410, Pub 572-K-9, 20 December 1973.

2. P. M. Besuner, D. O. Harris, and J. M. Thomas, "A Review of Fracture Mechanics Life Technology," NASA Contractor Report 3957, February 1986.

3. S. J. Hudak, Jr. and D. A. Russell, "A Comparison of Single-cycle Versus Multiple-Cycle Proof Testing Strategies," *Advanced Earth-to-Orbit Propulsion Technology 1988*, NASA Conference Publication 3012, Vol. 1, pp. 580-595, 1988.

4. A. L. Hallden, Rockwell International Internal Letter 9114-8062, 28 September 1979.

5. E. F. Tiffany and E. J. Masters, "Applied Fracture Mechanics," *Fracture Toughness Testing and Its Applications, ASTM STP 381*, 1965.

6. W. D. Buntin, "Concept and Conduct of Proof Testing of F-111 Production Aircraft," *Aeronautical Journal*, Vol. 76, No. 742, pp. 587-598, 1972.

7. J. M. Krafft, A. M. Sullivan, and R. W. Boyle, "Effect of Dimensions on Fast Fracture Instability of Notched Sheets," *Proc. of the Crack Propagation Symposium*, Cranfield, England, Vol. 1, 1961, pp. 8-26.

8. *Fracture Toughness Evaluation by R-Curve Methods, ASTM STP 527*, American Society for Testing and Materials, 1973.

9. D. P. Wilhem and M. M. Ratwani, "Application of the R-Curve Concept to Fatigue Crack Growth," *Trans. ASME, J. Engineering Materials and Technology*, Vol. 100, 1978, pp. 416-420.

10. K.-H. Schwalbe, "Some Properties of Stable Crack Growth," *Engineering Fracture Mechanics*, Vol. 11, 1979, pp. 331-342.

11. J. A. Begley and J. D. Landes, "The J-Integral as a Fracture Criterion," *Fracture Toughness, Part II, ASTM STP 514*, 1972, pp. 1-20.

12. J. D. Landes and J. A. Begley, "The Effect of Specimen Geometry on J_{Ic}," *Fracture Toughness, Part II, ASTM STP 514*, 1972, pp. 25-39.

13. J. R. Rice, "Mathematical Analysis in the Mechanics of Fracture," *Fracture*, Vol. 2, Academic Press, N.Y., 1968, pp. 191-311.

14. P. C. Paris, H. Tada, H. Ernst, and A. Zahorr, "Initial Experimental Investigation of Tearing Instability Theory," *Elastic-Plastic Fracture, ASTM STP 668*, 1979, pp. 251-265.

15. P. C. Paris, H. Tada, A. Zahorr, and H. Ernst, "Instability of the Tearing Mode of Elastic-Plastic Crack Growth," *Elastic-Plastic Fracture, ASTM STP 668*, 1979, pp. 5-36.

16. D. Shows, A. F. Liu, and J. FitzGerald, "Application of Resistance Curves to Crack at a Hole," *Fracture Mechanics: Fourteenth Symposium, Volume II: Testing and Applications, ASTM STP 791*, 1983, pp. II-87 - II-100.

17. G. A. Clarke, W. R. Andrews, P. C. Paris, and D. W. Schmidt, "Single Specimen Tests for J_{Ic} Determination," *Mechanics of Crack Growth, ASTM STP 590*, 1976, pp. 27-42.

18. C. W. Marschall and G. W. Wilkowski, "Effect of Cyclic Loads on Ductile Fracture Resistance," *Advances in Fracture and Fatigue for the 1990's, Vol. I: Load History Effects of Fracture Resistance*, PVP - Vol. 166, ASME Pressure Vessels and Piping Conference, Honolulu, Hawaii, July 1989, pp. 1-13.

19. G. E. Sutton and M. G. Vassilaros, "Influence of Partial Unloadings Range on the J_r-R Curves of ASTM A106 and 3-Ni Steels," *Fracture Mechanics: Seventeenth Volume, ASTM STP 905*, 1986, pp. 364-378.

20. J. A. Joyce, "Characterization of the Effects of Large Unloading Cycles on the Ductile Tearing Toughness of HSLA Steel," *Advances in Fracture and Fatigue for the 1990's, Vol. I: Load History Effects of Fracture Resistance*, PVP - Vol. 166, ASME Pressure Vessels and Piping Conference, Honolulu, Hawaii, July 1989, pp. 15-21.

21. F. W. Brust, J. J. McGowan, and S. N. Atluri, "A Combined Numerical/Experimental Study of Ductile Crack Growth After a Large Unloading, Using T^*, J, and CTOA Criteria," *Engineering Fracture Mechanics*, Vol. 23, No. 3, 1986, pp. 537-550.

22. F. W. Brust, M. Nakagaki, and S. N. Atluri, "Assessment of High Amplitude Cyclic Crack Growth Using a Near Crack Parameter," presented at ASME Pressure Vesels and Piping Conference, Honolulu, Hawaii, July 1989.

23. N. E. Dowling and J. A. Begley, "Fatigue Crack Growth During Gross Plasticity and the J-Integral," *Mechanics of Crack Growth, ASTM STP 590*, 1976, pp. 82-103.

24. R. C. McClung, "Applications of a Finite Element Analysis of Fatigue Crack Closure," *Advances in Fracture Research*, Proc. 7th Int. Conf. Fracture (ICF7), March 1989, Vol. 2, pp. 1257-1264.

25. S. Kaiser, "On the Relation Between Stable Crack Growth and Fatigue," *Fatigue of Engineering Materials and Structures*, Vol. 6, No. 1, 1983, pp. 33-49.

26. R. G. Forman, V. E. Kearney, and R. M. Engle, "Numerical Analysis of Crack Propagation in Cyclic-Loaded Structures," *Journal of Basic Engineering, Trans. ASME*, Vol. 89, September 1967, pp. 459-464.

27. K. Mogami, T. Hayashi, K. Ando, and N. Ogura, "Elastic-Plastic Cyclic J-R Curve and Tearing Instability Characteristics Under Cyclic Load," *Advances in Fracture and Fatigue for the 1990's, Vol. I: Load History Effects of Fracture Resistance*, PVP - Vol. 166, ASME Pressure Vessels and Piping Conference, Honolulu, Hawaii, July 1989, pp. 71-76.

28. H. Kobayashi, T. Kusumoto, and H. Nakazawa, "Cyclic J-R Curve and Upper Limit Characteristic of Fatigue Crack Growth in 2-1/2 Cr-Mo Steel," *Advances in Fracture and Fatigue for the 1990's, Vol. I: Load History Effects of Fracture Resistance*, PVP - Vol. 166, ASME Pressure Vessels and Piping Conference, Honolulu, Hawaii, July 1989, pp. 55-63.

29. T. W. Orange, "Method and Models for R-Curve Instability Calculations," NASA TM 100935, 1988.

30. V. Kumar, M. D. German, and C. F. Shih, "An Engineering Approach for Elastic-Plastic Fracture Analysis," EPRI Report NP-1931, July 1981.

31. R. A. Ainsworth, "The Assessment of Defects in Structures of Strain Hardening Material," *Engineering Fracture Mechanics*, Vol. 19, No. 4, 1984, pp. 633-642.

32. A. G. Miller, "J Estimation for Surface Defects," TPRD/B/0811/R86, Central Electricity Generating Board, July 1986.

33. D. M. Parks and Y.-Y. Wang, "Elastic-Plastic Analysis of Part-Through Surface Cracks," *Analytical, Numerical, and Experimental Aspects of Three Dimensional Fracture Processes*, AMD-Vol. 91, ASME, 1988, pp. 19-32.

34. R. A. Ainsworth, "Approximate Non-Linear Fracture Mechanics Calculations Using Reference Stress Techniques," *Innovative Approaches to Irradiation Damage and Fracture Analysis*, PVP - Vol. 170, ASME Pressure Vessels and Piping Conference, Honolulu, Hawaii, July 1989, pp. 13-20.

35. J. C. Newman, Jr., and I. S. Raju, "An Empirical Stress Intensity Factor Equation for the Surface Crack," *Engineering Fracture Mechanics*, Vol. 15, 1981, pp. 185-192.

36. N. E. Dowling, "*J*-Integral Estimates for Cracks in Infinite Bodies," *Engineering Fracture Mechanics*, Vol. 26, No. 3, 1987, pp. 333-348.

37. G. G. Trantina, H. G. deLorenzi, and W. W. Wilkening, "Three-Dimensional Elastic-Plastic Finite Element Analysis of Small Surface Cracks," *Engineering Fracture Mechanics*, Vol. 18, 1983, pp. 925-938.

38. D. E. McCabe, "Flaw Growth Analysis For 2219-T87 Aluminum Pressure Vessel Welds," Materials Engineering Associates Report No. MEA-2321, prepared for Martin Marietta Aerospace, November 1988.

39. C. S. White, R. O. Ritchie, and D. M. Parks, "Ductile Growth of Part-Through Surface Cracks: Experiment and Analysis," *Elastic-Plastic Fracture: Second Symposium, Volume I -- Inelastic Crack Analysis, ASTM STP 803*, 1983, pp. I-384 - I-409.

NASA

Report Documentation Page

1. Report No
NASA CR-4318

2. Government Accession No.

3. Recipient's Catalog No.

4. Title and Subtitle
A Comparison of Single-Cycle Versus Multiple-Cycle Proof Testing Strategies

5. Report Date
August 1990

6. Performing Organization Code

7. Author(s)
S. J. Hudak, Jr., R. C. McClung, M. L. Bartlett, J. H. FitzGerald, and D. A. Russell (Rocketdyne)

8. Performing Organization Report No

10. Work Unit No.
M-643

9. Performing Organization Name and Address
Southwest Research Institute
6220 Culebra Road
San Antonio, Texas 78228-0510

11. Contract or Grant No
NAS8-37451

13. Type of Report and Period Covered
Interim Report
(November 1987-August 1989)

12. Sponsoring Agency Name and Address
NASA-George C. Marshall Space Flight Center
MSFC, Alabama 35812

14. Sponsoring Agency Code

15. Supplementary Notes
Subcontract support from Rocketdyne Division, Rockwell International
6633 Canoga Avenue
Canoga Park, California 91303

16. Abstract
An evaluation of single-cycle and multiple-cycle proof testing (MCPT) strategies for SSME components is described. Rocketdyne experience with MCPT is briefly reviewed. Data for initial sizes and shapes of actual SSME hardware defects are analyzed statistically. Closed-form estimates of the *J*-integral for surface flaws are derived with a modified reference stress method. The results of load- and displacement-controlled stable crack growth tests on thin IN-718 plates with deep surface flaws are summarized. A *J*-resistance curve for the surface-cracked configuration is developed and compared with data from thick compact tension specimens. The potential for further crack growth during large unload/reload cycles is discussed, highlighting conflicting data in the literature. A simple model for ductile crack growth during MCPT based on the *J*-resistance curve is used to study the potential effects of key variables. The projected changes in the crack size distribution during MCPT depend on the interactions between several key parameters, including the number of proof cycles, the nature of the resistance curve, the initial crack size distribution, the component boundary conditions (load vs. displacement control), and the magnitude of the applied load or displacement. The relative advantages of single-cycle and multiple-cycle proof testing appear to be specific, therefore, to individual component geometry, material, and loading.

17. Key Words (Suggested by Author(s))
proof testing, elastic-plastic fracture mechanics, resistance curves, surface cracks, J-integral, crack size distribution

18. Distribution Statement
Unclassified - Unlimited
Subject Category: 39

19. Security Classif (of this report)
Unclassified

20. Security Classif. (of this page)
Unclassified

21. No. of pages
76

22. Price
A05

NASA FORM 1626 OCT 86
For sale by the National Technical Information Service, Springfield, VA 22161-2171
NASA-Langley, 1990

BULK [illegible]
POSTAGE [illegible]
NAS[illegible]
Permit N[illegible]

NASA

POSTMASTER: If Unde[illegible]
Postal [illegible]